Chemical Evolution History of MaNGA Galaxies

Artemi Camps-Fariña[1,2] , Sebastián F. Sánchez[1] , Alfredo Mejía-Narváez[1] , Eduardo Lacerda[1] , Leticia Carigi[1] ,
Gustavo Bruzual[3] , Paola Alvarez-Hurtado[1] , Niv Drory[4] , Richard R. Lane[5] , Nicholas Fraser Boardman[6], and
Guillermo A. Blanc[7,8]

[1] Instituto de Astronomía, Universidad Nacional Autónoma de México, Apartado Postal 70-264, CP 04510 Ciudad de México, México; arcamps@ucm.es
[2] Departamento de Física de la Tierra y Astrofísica, Universidad Complutense de Madrid, E-28040 Madrid, Spain
[3] Instituto de Radioastronomía y Astrofísica, IRyA, UNAM, Morelia, México
[4] McDonald Observatory, The University of Texas at Austin, 1 University Station, Austin, TX 78712, USA
[5] Centro de Investigación en Astronomía, Universidad Bernardo O'Higgins, Avenida Viel 1497, Santiago, Chile
[6] Department of Physics & Astronomy, University of Utah, Salt Lake City, UT 84112, USA
[7] The Observatories of the Carnegie Institution for Science, 813 Santa Barbara Street, Pasadena, CA 91101, USA
[8] Departamento de Astronomía, Universidad de Chile, Casilla 36-D, Santiago, Chile
Received 2021 December 27; revised 2022 April 26; accepted 2022 May 3; published 2022 July 1

Abstract

We show the results of a study using the spectral synthesis technique study for the full MaNGA sample showing their chemical enrichment history (ChEH) as well as the evolution of the stellar mass–metallicity relation (MZR) over cosmic time. We find that the more massive galaxies became enriched first and the lower-mass galaxies did so later, producing a change in the MZR that becomes shallower in time. Separating the sample into morphology and star-forming status bins, some particularly interesting results appear: The mass dependence of the MZR becomes less relevant for later morphological types, to the extent that it inverts for Sd/Irr galaxies, suggesting that morphology is at least as important a factor as mass in the chemical evolution. The MZR for the full sample shows a flattening at the high-mass end and another in the low-mass range, but the former only appears for retired galaxies, while the latter only appears for star-forming galaxies. We also find that the average metallicity gradient is currently negative for all mass bins, but for low-mass galaxies, it was inverted at some point in the past, before which all galaxies had a positive gradient. We also compare how diverse the ChEHs are in the different bins we considered, as well as what primarily drives the diversity: By how much galaxies become enriched, or how quickly they do so.

Unified Astronomy Thesaurus concepts: Galaxies (573); Chemical abundances (224); Galaxy chemical evolution (580)

1. Introduction

Galaxy evolution remains one of the key problems to be solved in astrophysics. It involves many physical processes that take place at diverse scales, from star formation feedback to interaction between galaxies. The composition of each galaxy is also very important: the total mass of stars and their ages, as well as the amount of gas and how enriched it is by metals all have an impact on the evolution of their host galaxy.

The chemical content of a galaxy offers a unique view into how the evolutionary processes of galaxies work. Practically all elements heavier than hydrogen and helium are produced as the end result of star formation and evolution (e.g., Kobayashi et al. 2020). The quantity of metals present in a galaxy and its distribution are tied to star formation episodes, and more fundamentally, to stellar evolution (Yates et al. 2013, and references therein). Other processes, such as inflows, outflows, and mixing (Tremonti et al. 2004; Lilly et al. 2013; Minchev et al. 2013, 2014; Maiolino & Mannucci 2019), can also influence the values of the metallicity. Disentangling the history of the chemical enrichment in a galaxy is therefore a great way to probe into the history of galaxy evolution.

Many studies regarding the metallicity in galaxies focus on the nebular metallicity, that is, measuring the metal content of ionized gas using emission line ratios and following known calibrations (Tremonti et al. 2004; Mannucci et al. 2010; Dayal et al. 2013; Sánchez et al. 2013; Barrera-Ballesteros et al. 2017). The other way to measure metallicity is to analyze the spectra of the stellar population to derive the metallicity of the interstellar medium (ISM) in which they were formed, as we do in this article (Gallazzi et al. 2005; Panter et al. 2007; Kirby et al. 2013; González Delgado et al. 2014; Leethochawalit et al. 2019; Zhuang et al. 2021). These two methods are complementary. The nebular metallicity offers a snapshot of the current state of the cumulative chemical enrichment in a galaxy and has the advantage of being easier to measure as a result of relying on emission lines, although this also has some drawbacks (Kewley & Ellison 2008; López-Sánchez et al. 2012; Blanc et al. 2015; Maiolino & Mannucci 2019).

Stellar metallicity, on the other hand, requires a more detailed analysis to fit the spectra to templates to derive the metallicity values. However, it has the unique capacity of tracing the metallicity at earlier cosmological times. The reason for this is that the metallicity of the ISM at the time of birth for a star is effectively locked-in in the star, allowing us to associate stellar metallicity to stellar age by tracing the varying values for different ages, and therefore different look-back times (LBT). Stars continuously produce metals throughout their lifetime, but these remain at their central region for the majority of their lifetime, while the atmospheric layers dominate the emission. Thanks to these phenomena, we can

measure the chemical enrichment over time for each galaxy in our sample.

In order to study the chemical enrichment of galaxies using nebular metallicity, we need to measure galaxies at different redshifts to infer a chemical enrichment history (ChEH; Lu et al. 2015; Cullen et al. 2019; Pharo et al. 2019; Urrutia et al. 2019). This has the advantage of not being tied to model-dependent fits, as is the case for stellar metallicity. However, it has the disadvantage of not tracing the evolution of the same group of galaxies, which makes it vulnerable to selection biases. One example is how the requirement for strong emission lines means that galaxies with strong star formation are generally selected. Additionally, direct-method nebular metallicities rely on the observation of weak auroral emission lines to be precise, which are difficult to observe at high redshifts. Strong line-based determinations of the nebular metallicity rely on empirical calibrators that are not guaranteed to be valid at all cosmic epochs and that have uncertainties regarding the absolute value of the metallicity (e.g., Kennicutt et al. 2003; Pérez-Montero & Díaz 2005; Kewley & Ellison 2008; Bresolin et al. 2009).

In this article, we present results for the evolution of the chemical enrichment of galaxies from the MaNGA survey (Bundy et al. 2015), a large sample of ∼10,000 galaxies, using the spectral synthesis technique. We study both the ChEH and the stellar mass–metallicity relation (MZR), which offer complementary insights into the evolution of the galaxies. The structure of this article is as follows: Section 2 describes the characteristics of the sample, the criteria used to refine it, and briefly, the data. In Section 3 we explain the method we applied to reduce and analyze the data. In Section 4 we show the results, the estimated ChEH (Section 4.1) and MZR (Section 4.2). Sections 4.3 and 4.4 show how these parameters change if they divide the sample depending on morphology or star-forming status (SFS). We also show how measuring the metallicity at different galactocentric radii affects the results (Section 4.5) and how similar the chemical enrichment histories are within the bins that we consider for the sample in terms of mass, morphology, and SFS (Section 4.6). Finally, in Section 5 we discuss the implications of the results, and in Section 6 we summarize our results.

2. Sample and Data

The MaNGA survey (Bundy et al. 2015) is one of the three projects of the fourth generation of the Sloan Digital Sky Survey (SDSS; York et al. 2000). It has recently completed its goal of observing a representative sample of over 10.000 galaxies in the nearby universe ($\langle z \rangle \sim 0.03$) with IFUs, obtaining a large sample of spatially resolved spectroscopic data. It uses the BOSS spectrographs (Smee et al. 2013) on the 2.5 m Sloan Telescope at Apache Point Observatory (Gunn et al. 2006). The adopted IFUs consist of a set of bundles of optical fibers connected to the spectrographs, with a different number of fibers that varies from 19 fibers (covering $12''$ in diameter) to 127 fibers (covering $32''$ in diameter). These are used for different targets depending on their extension (Drory et al. 2015). The instrument also includes 12 sets of 7 fiber mini-bundles for flux calibration and 92 individual fibers used for sky subtraction (Yan et al. 2016).

The spectral data cover a wavelength range from 3600 to 10.300 Å at a resolution of $R \sim 2000$. The raw data were processed using the MaNGA data reduction pipeline (DRP;

Law et al. 2016), which produces the data cubes we use in this work. The reduced data cubes have a point-spread function (PSF) of about $2.''5$ FWHM and a spaxel size of $0.''5$.

The MaNGA sample is comprised of a Primary sample, which selects galaxies that can be covered by the instrument out to 1.5 effective radii (Re) and consists of ∼2/3 of the objects, and a Secondary data sample, which comprises galaxies covered out to 2.5 Re and contains ∼1/3 of the objects. Selecting the galaxies via projected size inevitably introduces a bias. More massive, physically larger galaxies have higher redshifts, with the opposite effect occurring for physically small galaxies, which are located at a much closer distance. A color-enhanced sample was added to the survey to bolster the number of galaxies observed, which correspond to the more sparsely populated areas of the star-forming main sequence (SFMS) diagram, such as the green valley (GV) and low-mass red galaxies.

For this work, we have refined the mother sample of slightly more than 10,000 galaxies to suit our purpose better. First we remove galaxies that are viewed edge-on or are excessively inclined, as they would be less reliable in terms of the determination of their parameters (Ibarra-Medel et al. 2019). We chose to include only galaxies that are below 70° of inclination. We also removed galaxies whose emission lines indicated the presence of an active galactic nucleus (AGN), using the criteria from Lacerda et al. (2020). Our refined sample contains 9087 galaxies.

3. Analysis

The aperture of a single MaNGA fiber at the average redshift of the sample encompasses the light of thousands of stars added up. Therefore we can assume that the number of stars that contribute to each spectrum is a good sampling of the IMF. In this way, the observed spectrum is the sum of the emission of the stellar populations that correspond to the different individual episodes of star formation.

A composite spectrum of a specific region will vary depending on the star formation history (SFH) of the population, the metal composition of the ISM in which stars of different ages formed, and the present-day dust extinction. The process of fitting a library of spectra to the observations to recover the composition of the underlying stellar population is called the spectral synthesis or fossil record technique. This process allows us to probe into the past of a galaxy from the features left behind in the current stellar population.

3.1. PYPIPE3D

PYPYPE3D (Lacerda et al. 2022) is a new implementation of the FIT3D package (Sánchez 2006) adopted by the pipeline PIPE3D (Sánchez et al. 2016a, 2016b). This code allows the user to analyze IFU data of galaxies, obtaining the full information of the ionized gas emission lines as well as applying the spectral synthesis technique to the stellar spectra to obtain spatially resolved information on the galaxy composition and history. It is a port of the previous version to PYTHON 3, which makes it run about five times faster on average while producing consistent results (Lacerda et al. 2022).

The process of fitting the stellar templates yields the main product that the pipeline will use to derive the physical properties, i.e., the fraction of light corresponding to each

template at each spatial position. This fraction of light informs us of the current contribution that each population has toward the emission. We can correct this fraction based on the predicted loss of mass due to the stars that have died since the time the population was produced, i.e., its age. This has an effect by which the older a stellar population is, the larger proportion of the stars they consist of will have died compared to the more recent ones. This is compounded by the fact that the changes to a composite spectrum due to age become less prominent for older populations. Because of this, stellar template libraries tend not to have a constant sampling on their ages, with a finer sampling for the younger populations (see Walcher et al. 2011; Conroy 2013; Ibarra-Medel et al. 2016).

Using the corrected fractions of mass, we can obtain the number of stars that formed at each time, and thus, the SFH whose cumulative function is the stellar mass assembly history (MAH; Panter et al. 2003; Cid Fernandes et al. 2013; García-Benito et al. 2017). If we instead probe the metallicity, we can obtain the spatial distribution of metallicity values, which is usually studied as the radial metallicity gradient (Cid Fernandes et al. 2013; Sánchez-Blázquez et al. 2014; González Delgado et al. 2015; Sánchez 2020; Sánchez et al. 2021). The values of the metallicity that we calculate are averages of the populations, and as such, they can be weighted by stellar mass or by luminosity. In this work we weight the populations by their luminosity. Exploring the temporal and metallicity information for stars of different ages, the stellar metallicity is derived at different cosmic times, allowing us to obtain the ChEH, which is the main property we are interested in for this article.

Spectral synthesis analysis is a powerful tool to infer the past evolution of galaxies, but there are some caveats that need to be kept in mind in order to properly assess the results it provides. The reliability of the spectral fit is rife with degeneracies, the most important of which is the age–metallicity degeneracy, by which an older population has similar emission features as those of a more metallic one. The precision of the age determination also worsens as the age of the templates required to fit the spectrum increases, making the higher LBT data points less reliable in general. Walcher et al. (2011) and Sánchez-Blázquez et al. (2011) are useful references for how these degeneracies affect the results.

3.1.1. Stellar Population Libraries

The stellar population templates used for this article were constructed using the MaStar stellar library (SDSS DR15; Yan et al. 2019). The implementation of MaStar is ideal since the spectra of the stars in this library were observed with the same instrument as was used to obtain the MaNGA data (Drory et al. 2015). The template of stellar populations was created using the GALAXEV[9] (Bruzual & Charlot 2003; Yan & Wang 2010) stellar population synthesis code, assuming a Salpeter initial mass function (IMF; Salpeter 1955) and the PARSEC set of isochrones (Bressan et al. 2012). The code generates a grid of 3360 SSP templates that comprises 210 ages and 16 metallicities. This is by far too large to be used as the base of the fitting procedure for the reasons discussed in Sanchez et al. (2016) and Lacerda et al. (submitted). From this library, we select a subset of SSPs with a reasonable sampling of the age–metallicity space, as described in Sanchez et al. (in prep.)

This final library is named sLOG. It covers a total of seven metallicities and 39 ages, consisting of a total of 273 templates. The distribution of the templates in the parameter spaces is also shown in Appendix A, in which a comparison between different samplings of the stellar ages is also presented.

As already discussed in Sánchez et al. (2018), this library is different than the one adopted in previous explorations of the MaNGA data set using Pipe3D (e.g., Ibarra-Medel et al. 2016; Sánchez et al. 2017, 2019; Cano-Díaz et al. 2019) and a previous exploration of the ChEH using the CALIFA data set (Camps-Fariña et al. 2021, hereafter CF21). In these cases we adopted the GSD library (GSD156; Cid Fernandes et al. 2013). For completeness, we have included the main figures and results discussed in this article using this former library in Appendix B. This will allow the user a direct comparison with the results presented in CF21.

3.2. Averaging the Properties

The output of PYPIPE3D allows us to obtain the individual ChEHs for each galaxy. Following CF21, (i) we can compare the chemical evolution of the galaxies depending on their mass, morphology, and SFS. In addition, (ii) we obtain the MZR at different cosmological times using the information contained in a set of ChEHs averaged within the mass bins. An individual ChEH contains metallicity-time data points. By separating them into mass bins and averaging them, we have data points in the metallicity-time-mass parameter space. The MZR is immediately obtained by selecting a slice in the time dimension, yielding mass–metallicity data points at a particular time.

An average of the ChEH of a set of galaxies has to be done in a particular manner, taking into account some caveats and details (as already highlighted in CF21). One of the main concerns is that galaxies in the sample lie at different redshifts ($z \sim 0.01$–0.15 for the MaNGA sample), which means that the light-travel time (LTT) differs between them. When we fit the spectra of stellar population templates to the light we receive from the galaxy, LTT is not taken into account (except for the redshift effect). Correcting for this is trivial. We only need to add the LTT (given by the redshift via the adopted cosmology) to the ages. This, however, introduces two problems: first, the coverage in LBT is not uniform: Only nearby galaxies cover the more recent LBTs. Second, the sampling in time differs slightly between galaxies. The first caveat can be mitigated by limiting the LBT range to avoid the latest times, which are only represented by a handful of galaxies (not being representative of the full population). The second caveat can be solved by interpolating the individual ChEHs.

The averaging process itself is conducted in two steps. In the first step, we scale the ChEHs in each group (mass bins, mass and morphology bins, or mass and star formation rate bins for this work) to a characteristic metallicity of the group (the average of the currently observed metallicities). In the second step, we average the scaled ChEHs, which yields the representative ChEH for the group. The reason we do this is the nonhomogeneous coverage of the LBT, which means that not all galaxies contribute to all the times in the LBT. Thus, if we performed an average at each time value using only the galaxies that contribute there, we could introduce spurious behaviors into the ChEH. As an example, consider a very low metallicity galaxy that only contributed to the earlier half of the LBT range. A simple averaging would result in the anomalous
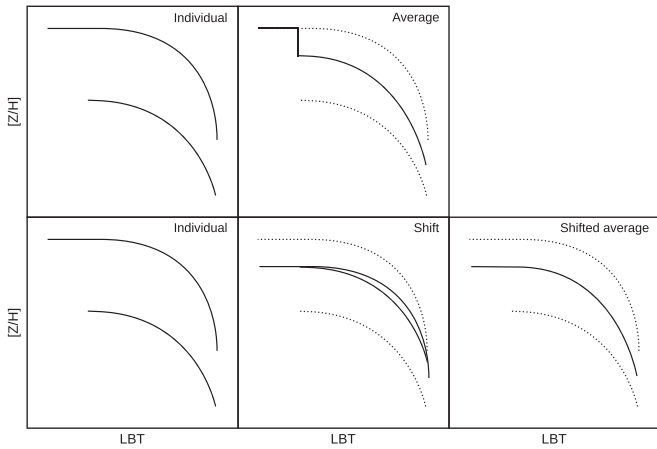
Figure 1. Schematic of how the two-step averaging technique used in this article can prevent artifacts on the shape of the average ChEH by shifting the galaxies to the average of their current metallicity first.

Figure 2. Distribution of the galaxies in the working sample of this article in their morphology bins. The Sd bin includes irregular galaxies. They indicated here in lighter gray.

galaxy lowering the average value of the metallicity only at these times, artificially inducing a growth in metallicity that is not representative of the group. By scaling the ChEHs first, the anomalous galaxy's effect on the average ChEH is not restricted to a specific part of the LBT range. This is a better approximation of the average that we would obtain if we had measurements for all galaxies at all times. In Figure 1 we show a schematic of how galaxies at different redshift can produce artifacts in the average ChEH and how the two-step averaging technique prevents them. The caveat is that the current metallicity of the averaged ChEH is no longer the same as if we averaged the currently observed metallicities in all the sample.

Another advantage of performing the averaging in this manner is that we can separate the sources of the variance within the group. The variance in the current values of the individual ChEH represents the offset between them, while the variance after shifting them is mainly due to the different rates at which they become enriched. This allows us to study whether a group of galaxies has similar growth patterns, but very different values of their current metallicity, or vice versa, whether their average metallicity values are similar, but have been enriched at a very different rate.

It is worth noting that there is a difference in how we perform the average compared to CF21. In that article, to perform the scaling, rather than taking the currently observed value for each ChEH at their full LBT range, we took the average value over the LBT range in which all galaxies had metallicity values. For the MaNGA sample, given the higher number of galaxies and a wider range of redshifts, this range is short and biased toward earlier LBT, where most galaxies were still in the initial enrichment process. The reason for this difference between the samples is the much narrower range in redshift that the CALIFA sample covers ($z \sim 0.005 - 0.03$) compared to MaNGA ($z \sim 0.01 - 0.15$).

3.3. Morphology Classification

In order to study how morphology affects the chemical enrichment, we need a catalog for the morphology of the galaxies in our sample. Current publicly available catalogs only contain the galaxies that are included in the releases up to DR15, representing about 4700, which is fewer than half the galax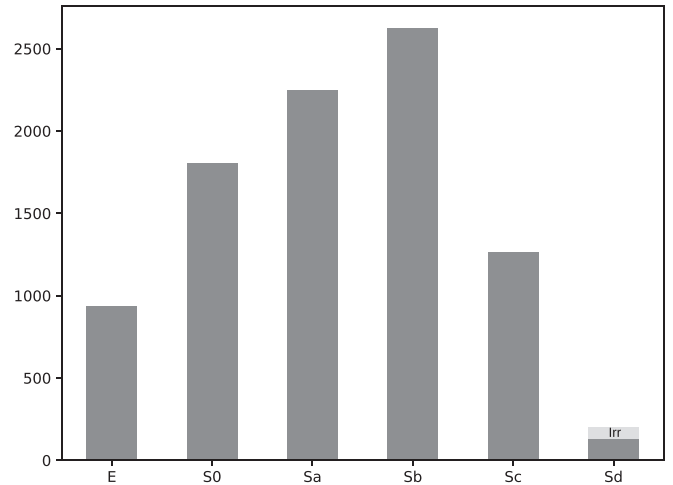ies available in the full sample. For the purposes of this article, we do not need a highly accurate determination of the morphology for each individual galaxy. It is enough if we have a consistent classification in terms of statistical properties.

For this purpose, we use the morphological classification provided by Sanchez et al. (submitted). This classification is based on a automatic machine-learning algorithm that uses as a training and testing sample the morphology determinations provided for a sample of $\sim$6000 galaxies included in the SDSS VAC catalog by Hernández-Toledo et al. (2010).[10] In Figure 2 we show the resulting distribution of the galaxies in the refined sample in the morphology bins used in this article.

4. Results

The analysis described before provides two main products: (i) the ChEH, which shows how the metallicity has changed for a particular group of galaxies through cosmic times; and (ii) the MZR, which shows the distribution of metallicities as a function of the mass of a population of galaxies at a certain cosmological time. In addition, we obtain the variance in both the currently observed value of the metallicity and the variance in the shape of the ChEH.

4.1. Chemical Enrichment History

In Figure 3 we show the average ChEH for the full sample as well as the SFH for different mass bins. We find a clear segregation of the average ChEH in the metallicity axis, with no mass bin crossing the ChEH of any other along all cosmic times. It is clearly seen that the more massive galaxies are also the ones that have the higher metallicity content at any cosmological time on average. However, this is not necessarily the case if we consider individual galaxies. It is possible for a galaxy from a lower-mass bin to have higher metallicity than one from a higher-mass bin.

There is also a change in the shape of the average ChEHs that varies with the mass of the galaxies. Less massive galaxies show a clear ongoing increase in metallicity, whereas the more massive galaxies have a shallower shape that is almost flat for the most massive ones. This is readily apparent from how the

---

[10] https://data.sdss.org/sas/dr16/manga/morphology/manga_visual_morpho/1.0.1/
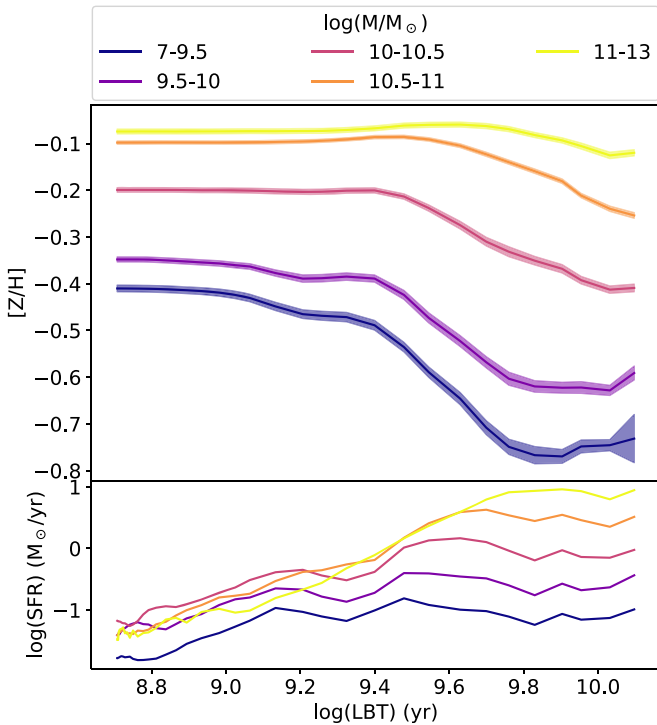
Figure 3. Chemical enrichment histories (top panel) and SFHs (bottom panel) of all the galaxies in our sample binned into five stellar masses (colors). For each solid line, which represents the average distribution, the shaded areas correspond to the bootstrapped error of the mean (i.e., the range of metallicities covered within each bin has been explicitly removed).

Figure 4. Evolution of the MZR along the cosmological time (bottom panel) and stellar mass distribution of the galaxies in our sample as currently observed (top panel). Shaded areas in the bottom panel represent the bootstrapped error for each ChEH derived by the averaging algorithm.

gap between them becomes narrower toward recent cosmic times.

The SFH also shows a correlation with stellar mass. The more massive galaxies have a higher SFR at earlier times. They present a steeper negative slope, and the less massive galaxies show a lower SFR along all cosmological times and a flatter distribution. This is in line with Panter et al. (2007), Pérez-González et al. (2008), Husemann et al. (2010), Pérez et al. (2013), Sánchez et al. (2018), and Sánchez (2020) and shows how the more massive galaxies had a very high SFR at early times in contrast with low-mass ones. The latter continue to steadily form stars on average.

4.2. Evolution of the MZR

In Figure 4 we show the MZR at different cosmic times. The main features observed are consistent with those observed in Figure 3. The slope of the MZR is always positive toward higher mass, showing that, at all times, the more massive galaxies have higher metallicities. The value of the slope itself, however, changes along cosmological time, becoming shallower toward recent times. There is a clear delay in the enrichment due to the mass, observed especially around the 5 Gyr MZR. At this time, the most massive galaxies have already reached their metallicity asymptotic value. On the other hand, low-mass galaxies have not significantly increased their metallicities at this time compared to the higher LBTs sampled (i.e., between 5 and 11 Gyr). This is a consequence of high-mass galaxies becoming enriched earlier than low-mass ones. This result is in line with what we found in the previous section, with the higher-mass galaxies having shallower
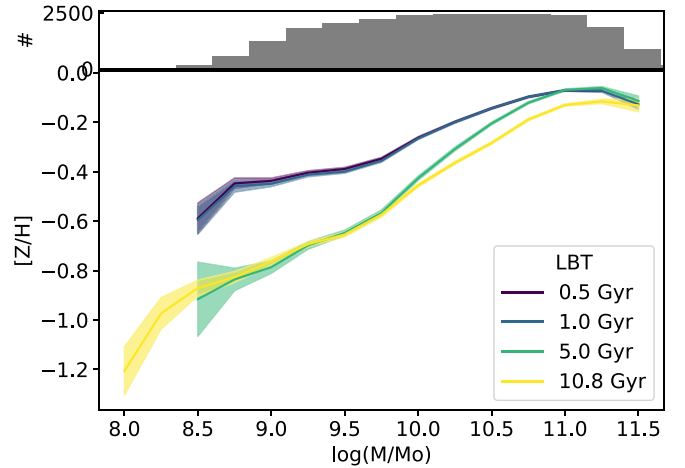
ChEHs. High-mass galaxies became enriched very early on, while lower-mass galaxies have steadily been catching up to them, thus producing the observed change in slope.

The MZR shows a flattening toward high masses, which would imply a kind of saturation regarding the enrichment of the medium. This flattening has been observed before in the nebular MZR (Tremonti et al. 2004; Kewley & Ellison 2008; Rosales-Ortega et al. 2012; Sánchez et al. 2014; Barrera-Ballesteros et al. 2017; Sánchez et al. 2019; Blanc et al. 2019). Among the proposed explanations for this observational result, those with the strongest support are related to the effect of metal-rich outflows and metal-poor inflows in shaping this distribution (e.g., Gallazzi et al. 2005; González Delgado et al. 2014; Sánchez Almeida et al. 2014; Barrera-Ballesteros et al. 2017; Sánchez et al. 2018; Lacerda et al. 2020). Zahid et al. (2014) proposed that the flattening is the result of the saturation of the metal content in the gas. This occurs once the metallicity reaches a value such that the metal mass that is locked up in newly formed low-mass stars is similar to the metal mass produced in newly formed massive stars.

The low-mass regime, below $\sim 10^{9.7} \, M_{\odot}$, also appears to flatten, especially at recent times, but to a lesser extent than for the high-mass range. This feature has been observed previously in Gallazzi et al. (2005), Kirby et al. (2013), Leethochawalit et al. (2019), and Zhuang et al. (2021) for stellar metallicity and in Kashino et al. (2016) and Blanc et al. (2019) for nebular metallicity. It is also consistent with some high-resolution galaxy simulations (Schaye et al. 2015; Ma et al. 2016; Christensen et al. 2016, 2018), which show a flatter MZR for the low-mass regime under $10^{9.5} \, M_{\odot}$. There are, however, other studies in nebular metallicity in which the flattening is not observed, such as Lee et al. (2006), Berg et al. (2012), and Zahid et al. (2012). Blanc et al. (2019) discussed these discrepancies and how consistent this feature is, which they attribute to a characteristic mass ($10^{9.5} \, M_{\odot}$) above which the efficiency of metal-removal processes drops. For very low stellar masses, studies by Kirby et al. (2013) and Zhuang et al. (2021) find that the stellar MZR has a break compared to those above $\sim 10^9 \, M_{\odot}$.

One thing to note is that the mass at which the MZR steepens does not appear to change with LBT, which is especially
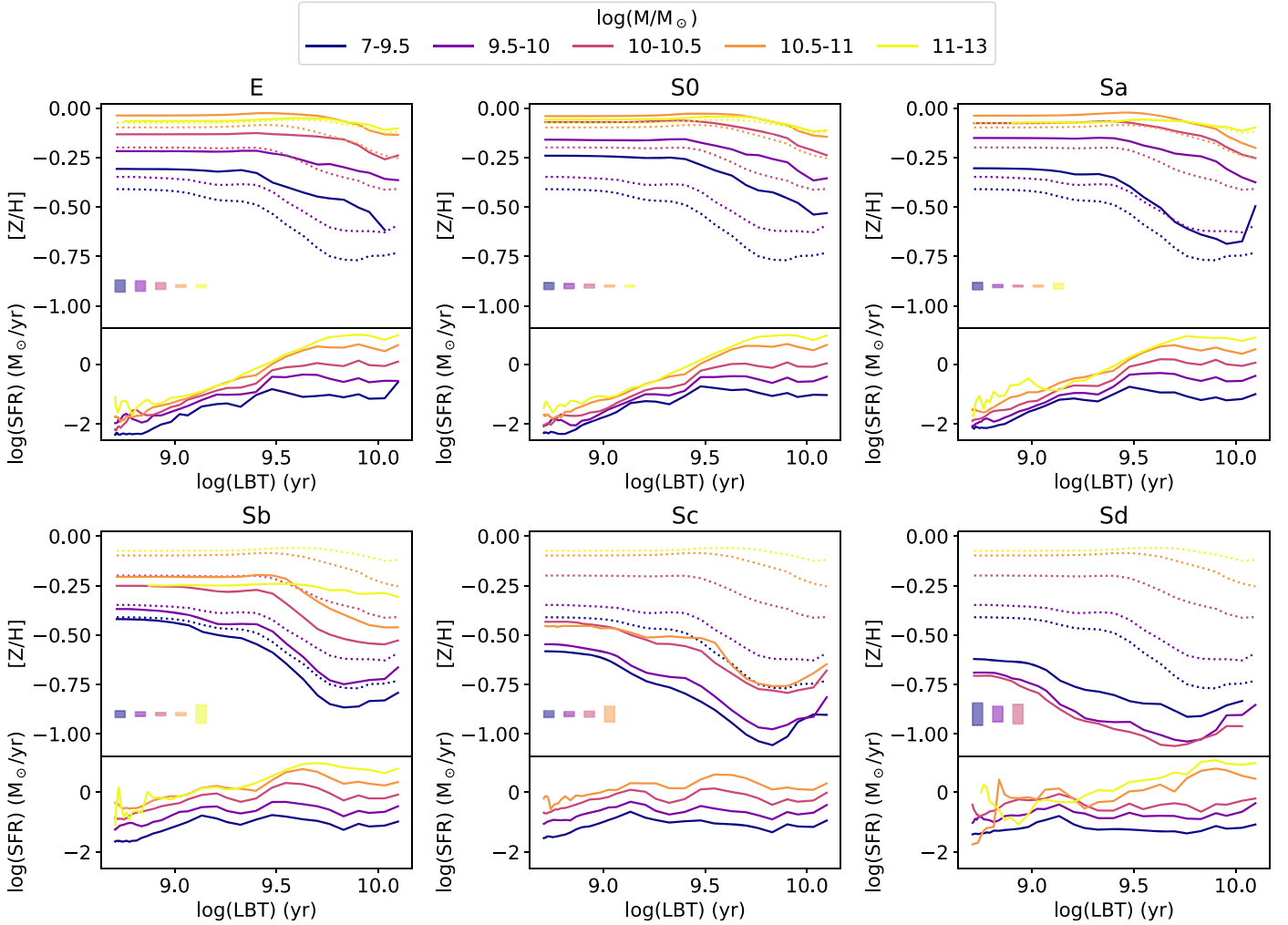
Figure 5. Chemical enrichment histories (top of each panel) and SFHs (bottom of each panel) of galaxies in our sample segregated by morphology. The dotted lines correspond to the ChEHs from Figure 3, which represent the full sample, shown here for the sake of comparison. The shaded areas show the average bootstrapped error for each ChEH in the same colors.

apparent comparing the 5 and 10.8 Gyr MZR. The two are practically the same up to $\sim10^{9.8}~M_\odot$, at which point the 5 Gyr MZR steepens. The fact that the turn-up mass remains constant in time supports the hypothesis that it is the characteristic stellar mass at which the gas removal processes become less efficient.

Another explanation for the flattening that must be taken into account for our study compared to others such as Tremonti et al. (2004) is that we are using stellar metallicity instead of nebular metallicity. We obtain our values from the fitting of stellar population templates, and therefore we are limited to the metallicity values that we can obtain by the parameter space covered by the templates. This can potentially produce a flattening of the MZR as the measured values of the metallicity approach the edge values of the stellar template library. The figures in Appendices B and C are helpful to assess whether this is the case for our results, as they show the MZR obtained by using a different stellar template library, which has a narrower range in metallicity compared to MaStar. In general, the narrower metallicity range creates quantitative differences, but not many qualitative ones. There does not appear to be a saturation effect such that bins with low metallicity cannot be distinguished, although the differences do become less clear.

4.3. Effect of Morphology

We explore how the morphology affects the chemical evolution in galaxies using the classification described in Section 3.3 to probe how the morphology of a galaxy affects its chemical evolution. By separating galaxies into both mass and morphological bins, we avoid the effect introduced by the mass-morphology correlation.

In Figures 5 and 6 we show the equivalent of Figures 3 and 4 but separated into morphology bins. In Figure 5 we can appreciate that earlier-type galaxies are generally more metallic than their late-type counterparts at a fixed mass. The same result is observed when exploring the shape of the ChEH. E galaxies have practically flat ChEHs for most mass bins, whereas spirals still present growth even at high masses (except for the $M^{11-13}~M_\odot$ bin) on average. More massive galaxies show this change better than lower-mass ones, which are more similar in shape across morphology bins in general, especially from Sb to Sd. However, the low-mass bins of E-S0-Sa galaxies have higher metallicities than later types in the same mass bin.

This effect is mirrored in the SFH distributions, with the earlier-type galaxies having steeper slopes as they stopped
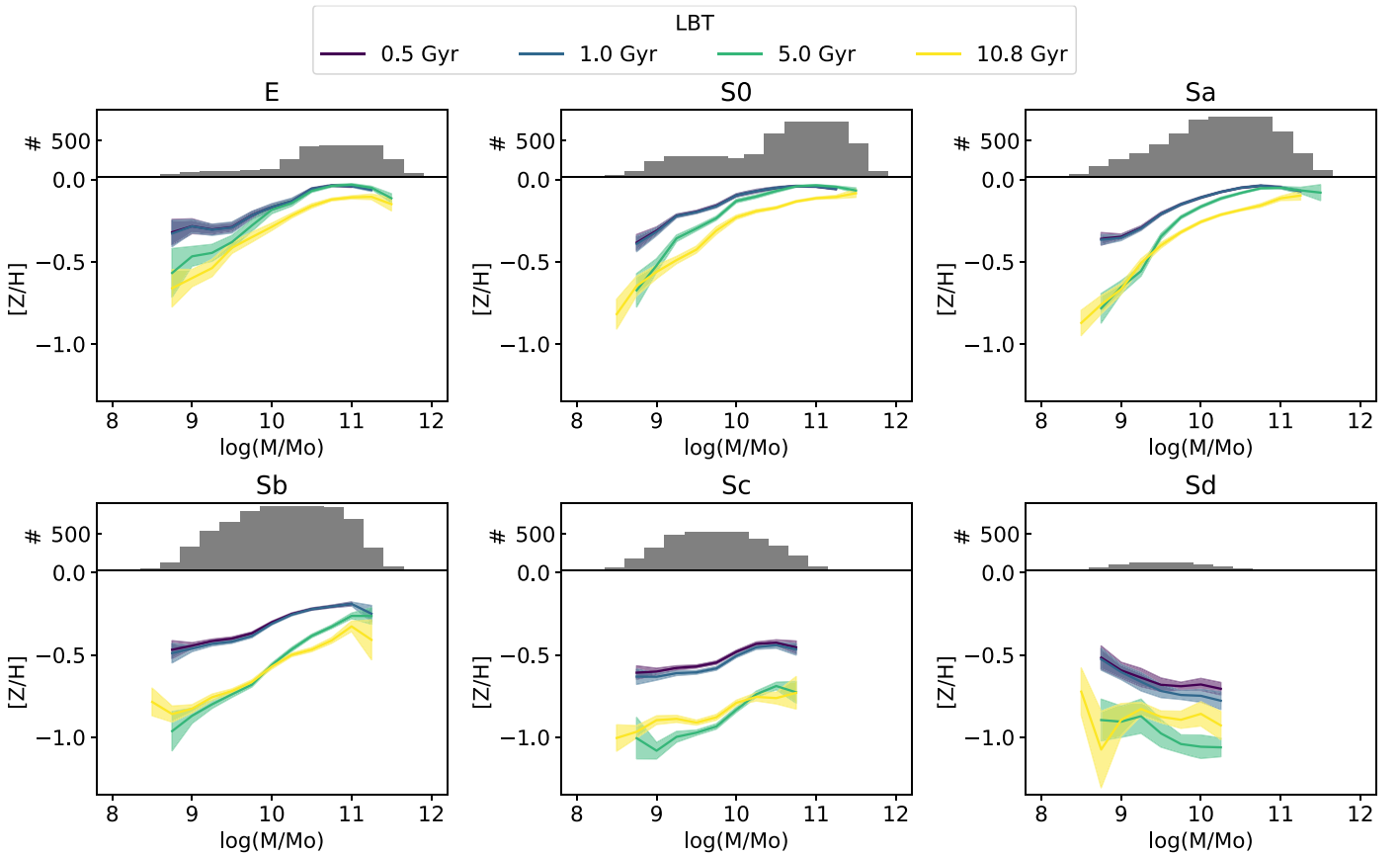
Figure 6. Evolution of the MZR along cosmological time for all galaxies in our sample separated by morphology. In the top panel of each plot, we show the distribution of galaxies along the mass range as currently observed. Shaded areas in the bottom panel represent the bootstrapped error.

forming stars early on. In contrast, later-type galaxies have flatter profiles, showing sustained star formation.

The MZR plots show results consistent with the ChEH plots, with earlier types having higher values of metallicity in general. However, the most interesting part of this figure lies in the shape of the MZR, which becomes progressively flatter toward later types, to the extent that Sd galaxies appear to have an inverted MZR. This can also be observed in the ChEHs, as the lowest-mass bin shows a higher metallicity than the higher-mass bins. The implication of this flattening of the slope depending on morphological type is that for late-type galaxies. the stellar mass is progressively less important in determining the current metallicity than the morphology. For Sd (and Sc to a lesser extent) galaxies, mass appears to have little impact on the metallicity enrichment on average.

The evolution of the MZR also changes between morphological types. The earlier types (E, S0, and Sa) become shallower as time passes and also show a delay in enrichment for lower-mass galaxies. The Sd galaxies, on the other hand, show neither a change in slope nor a delay in enrichment at all. The change in slope is caused by the delay in enrichment, and the fact that it is not observed in Sb and Sc galaxies indicates that the transitional LBT, where high-mass galaxies are already enriched but low-mass ones are not (~5 Gyr for the full sample), is shifted to more recent times for later-type galaxies. This shows how the delay in enrichment between galaxies is twofold: there is a delay due to mass, and another delay due to morphology. Thus, for two galaxies with equal stellar mass, the earlier-type galaxy will become enriched at a higher LBT. On the other hand, for two galaxies of the same morphological

type, the more massive galaxy will become enriched at a higher LBT. The Sd galaxies, however, show no change in slope and therefore have no delay in enrichment due to mass.

Considering that earlier types dominate the high-mass range and later types the low-mass range, this implies that the global change in shape seen in Figure 6 is not simply a result of mass regulating how fast galaxies evolve. Morphology appears to be at least as important.

4.4. Effect of the Star-forming Status

Next, we explore how the SFS relates to the evolution of the chemical enrichment. We define the SFS of our galaxies based on the equivalent width (EW) of the average Hα emission line, defined at the effective radius. This quantity has been proven to be a good discriminator of the SFS (Stasińska et al. 2008; Sánchez et al. 2014; Cano-Díaz et al. 2016; Espinosa-Ponce et al. 2020; Lacerda et al. 2020; Sánchez 2020; Sánchez et al. 2021), where an $EW_{H\alpha}$ value of 6 Å is shown to be a good value to separate star-forming galaxies from retired ones. In this article, we wish to separate into star-forming (SFG), green valley (GVG), and retired (RG) galaxies, so we take discriminating values following Lacerda et al. (2020) of

1. SFG: $EW_{H\alpha}$ (R_e) > 10 Å
2. GVG: 3 Å < $EW_{H\alpha}$ (R_e) < 10 Å
3. RG: $EW_{H\alpha}$ (R_e) < 3 Å.

In Figures 7 and 8 we show how the SFS affects the results. It is important to take into account that this separation is not independent of the morphology. As seen in the previous
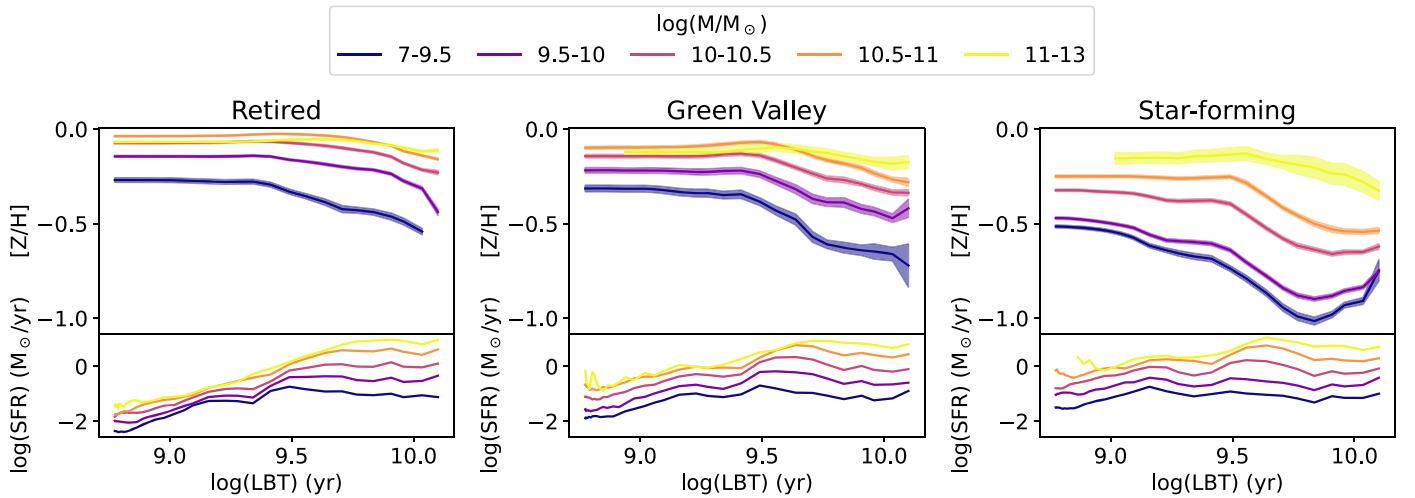
Figure 7. Chemical enrichment histories (top panel) and SFHs (bottom panel) of galaxies in our sample segregated by their current SFS. Shaded areas in the top panel represent the bootstrapped error.

section, late-type galaxies are more likely to have maintained a high SFR at current times, whereas early-type galaxies are likely to be retired. To claim that a particular feature is caused by the morphology or the SFS of galaxies in a group, the feature needs to be unique within its equivalent morphology and SFS bins. In other words, only a feature that (for example) appears in the SFG but not in late-type galaxies could be clearly claimed to be a result of SFS.

In this manner, we can see many expected results. SFG are generally less metallic and have steeper shapes in their ChEHs than GVG and RG, similarly to their dominant morphological components. An interesting feature that SFG show is a steeper enrichment between $10^{9.3}$ and $10^{9.7}$ yr, a feature that differs from RG and GVG. This slope change is stronger for higher-mass galaxies, with the two lowest-mass bins barely showing a change.

The MZR also shows the expected changes between SFS bins inherited from their morphology, with retired galaxies being more metallic than GVG and especially SFG. The RG show a much more prominent flattening at high masses compared to GVG, with SFG showing no high-mass flattening at all. The opposite happens for the low-mass flattening, which is absent in RG and GVG, but is clear in SFG. The evolution also shows differences: The delay in enrichment, which produces the change in slope, is more prominent in RG than in GVG and is absent in the SFG for the shown LBT values. As in Section 4.3, this implies that the transition time is closer to us for GVG and especially for SFG compared to RG.

Many of these features correlate with the corresponding features in morphology, but some features cannot be explained only through the SFS-morphology correlation. The low-mass flattening of the MZR is more prominent in the SFG than for any morphological bin. It could be argued that it is an effect of Sd galaxies dominating the lowest-mass range, but if we check the top panels of Figure 6, we can see that Sd galaxies are too rare to dominate Sbs even in the low-mass range. The evolution of the MZR for SFG is more similar to that of Sb galaxies. This is consistent with their numbers and likelihood of being in the SFG bin, but with a steeper slope and a more prominent low-mass flattening. The steeper slope can be explained as the effect of adding Sa galaxies, but the flattening appears to correlate more with the SFS, rather than being induced by the morphology.

The opposite happens for the high-mass flattening. This feature can be observed clearly for Sa galaxies, and to a lesser extent, also for Sb and Sc galaxies, although for the latter, the MZR is fairly flat overall. However, it is absent entirely in the SFG bin. Sa and Sb galaxies should be the dominant morphological types (especially at high stellar masses) in the SFG, so this clearly implies that the high-mass flattening of the MZR is strongly related to the SFS of galaxies. This link does not need to be direct. Following Zahid et al. (2014; see Section 4.2), the flattening would be the consequence of RG and GVG having already reached equilibrium metallicity, while most SFG have not done so.

4.5. Effect of the Radial Distance

Another parameter we can explore is the radial distance at which we measure the metallicity. So far, we have shown results measured at the Re, which is a good proxy for the global metallicity of a galaxy (e.g., González Delgado et al. 2014; Sánchez 2020), and therefore is a good scaling quantity to allow us to average galaxies of different sizes. Understanding how metallicity gradients form and evolve is a key aspect of galaxy evolution as it is the result of differential trends depending on environment (e.g., see Matteucci 2012; Kobayashi et al. 2020). Using the slope of the metallicity gradient, which is a parameter obtained from the PYPIPE3D pipeline, we can infer both the metallicity at the center and in the outskirts, which we have taken as 2 Re. This inference is only strictly valid if the gradient is linear, as the slope-fitting algorithm assumes. However, we consider it a good proxy for how the metallicity changes at different radial distances.

In Figures 9 and 10 we show the ChEHs and the MZR which result from measuring the metallicity at the center and at 2 Re. In general terms, the center tends to be more metallic and has a more pronounced evolution, whereas the ChEH has a similar shape for all mass bins in the outskirts. The gap between the ChEHs is also narrower. This is consistent with local downsizing, as the outskirts of galaxies are more similar in surface stellar mass density (Σ_*) compared to the center. Local downsizing is the extended version of downsizing, establishing a correlation between Σ_* and how fast a region's stellar population evolved, such that the more dense regions evolved faster than the lower-density regions. This is similar to how the
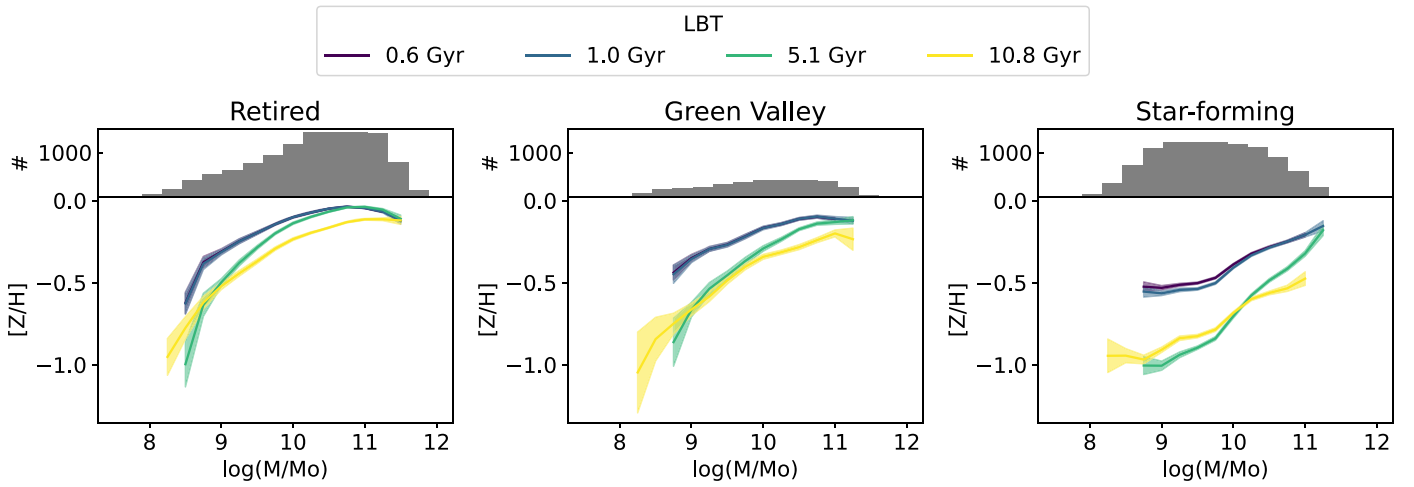
Figure 8. Evolution of the MZR along the cosmological time (bottom panel) and stellar mass distribution as currently observed (top panel) for all galaxies in our sample segregated by their current SFS. Shaded areas in the bottom panel represent the bootstrapped error.
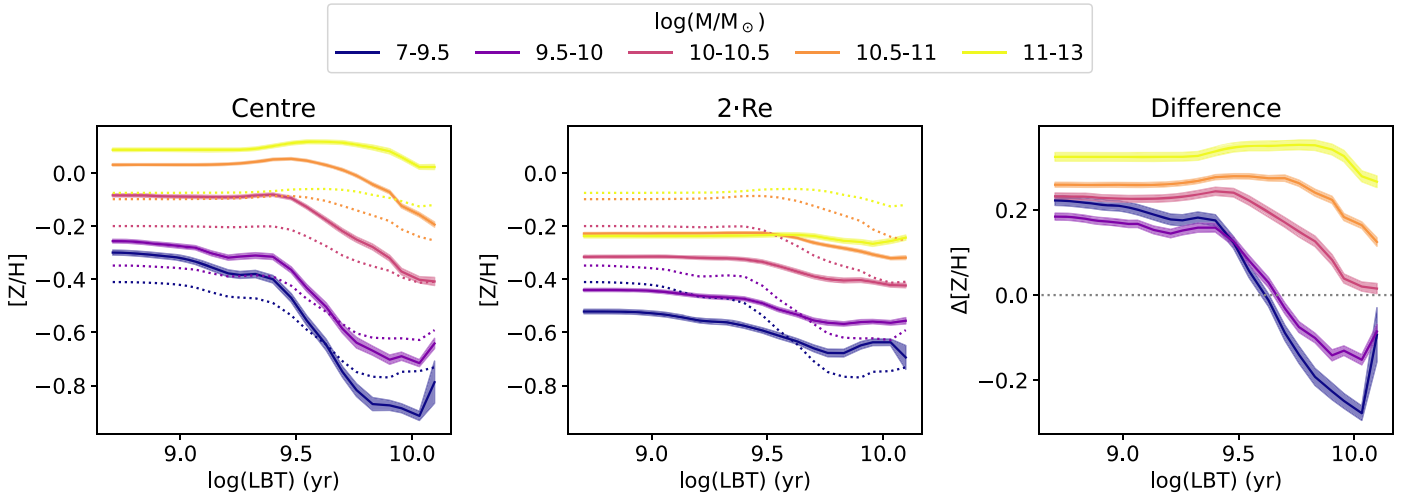

Figure 9. Chemical enrichment histories of galaxies in our sample measured at the center (left panel) and at twice the effective radius (center panel), as well as the difference between them (right panel). Shaded areas represent the bootstrapped error. The dotted lines in the left and center panels correspond to the ChEHs at the effective radius.
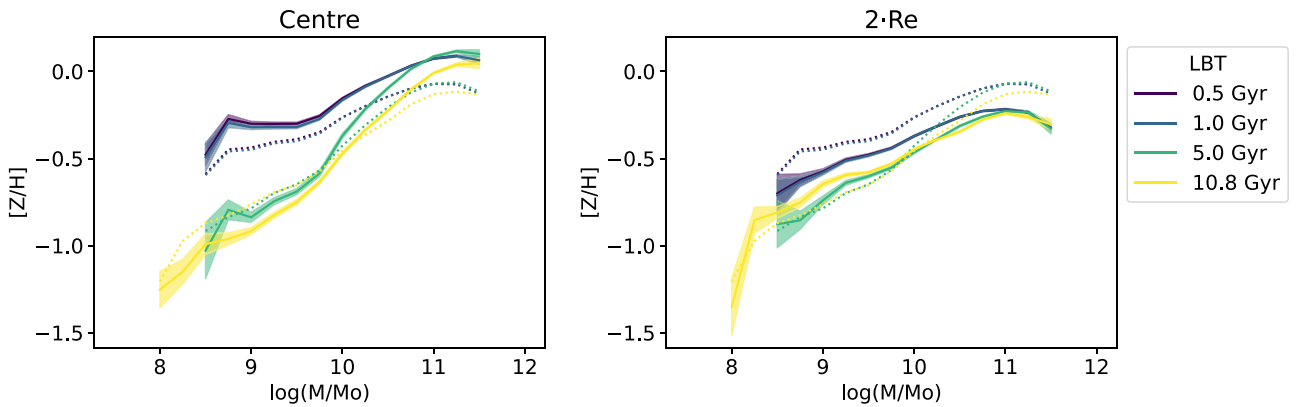
Figure 10. Evolution of the MZR along the cosmological time for all galaxies in our sample measured at the center (left panel) and at twice the effective radius (right panel). Shaded areas represent the bootstrapped error. The dotted lines in the left and center panels correspond to the MZR at the effective radius.

more massive galaxies assembled their stellar mass faster than low-mass galaxies (Pérez et al. 2013; Ibarra-Medel et al. 2016; García-Benito et al. 2017).

The MZR shows similar behaviors, with the change in shape over cosmic time being more evident at the center, but practically nonexistent in the outskirts. Generally, there are
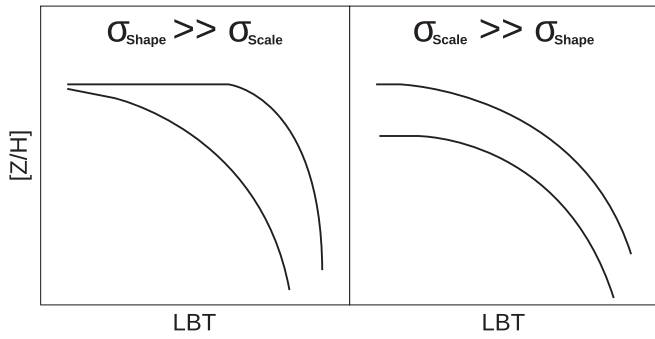
Figure 11. Diagram illustrating the difference between the two types of variance considered. In the left panel we show an example of two ChEHs with similar current metallicity, but different enrichment rates, whose average would have a higher σ_{Shape}. In the right panel we show the opposite case, with two ChEHs that are similar in their rate of enrichment (their shape), but have different values of the metallicity, such that the average of the two has a higher σ_{Scale}.

lower values of the metallicity and a flatter shape, which indicates that the differences in metallicity due to galaxy mass are less prominent. This shows once again that in their outskirts, galaxies are more similar for different stellar masses in terms of their chemical enrichment.

A particularly interesting feature can be seen in the ChEHs for lower galaxy masses. For recent cosmic times, all mass bins show a higher metallicity in the center than in the outskirts, a feature that is maintained at all LBTs for the high-mass bins. For masses below $10^{10}\,M_{\odot}$, on the other hand, the opposite trend is seen at earlier times, with a higher metallicity in the outskirts rather than at the center. As the stellar mass decreases, the positive gradient at early cosmic times is higher, and the switch to inside-out growth occurs at more recent cosmic times. This implies that the lower-mass galaxies shifted from an outside-in growth in metallicity to an inside-out growth approximately 4 Gyr ago ($10^{9.6}$ yr). It bears mention that the specific time for this inversion is likely to be heavily affected by the model for the stellar templates, so it should not be taken as a precise measurement (Ibarra-Medel et al. 2019; Sánchez 2020). Hidalgo et al. (2013) found that for four isolated dwarf galaxies, the stellar populations suggest an initial outside-in scenario, after which the SFR is quenched toward the center as the gas in the outskirts runs out. While these galaxies lie below our mass range at $M_* = 10^{6-7}\,M_{\odot}$, their behavior is consistent with our results.

Another interesting result can be seen in the flattening of the MZR at high and low masses. The high-mass flattening appears both at the center and in the outskirts, but it is more prominent in the latter. The low-mass flattening, on the other hand, is only clearly observed at the center and for recent times. Below $10^{9.5}$ $M_{\odot}$ and up to 1 Gyr in LBT, the MZR is completely flat at the center. This can be seen to a lesser extent in Figure 9 by comparing how the ChEH of the two lowest bins converges more at recent times in the center than in the outskirts.

4.6. Variances

Due to the unique way in which we have performed the averaging of the ChEHs, as described in Section 3.2, we can separate between two sources of variance that contribute to the standard deviation of the averaged ChEHs. One is dependent mostly on the current value of the metallicity for each ChEH, which we call σ_{Scale}, and the other is related to how diverse the

shapes of the ChEHs or the rates of enrichment are. The second one we call σ_{Shape}.

In Figure 11 we show a diagram that illustrates the meaning of the two types of variance for the ChEHs.

Comparing how the values of the standard deviations vary for the different groups considered in this article gives us a direct insight into the diversity in ChEHs and how it is affected by mass, morphology, and SFS.

In Figure 12 we show the two defined components of the variance for the galaxies in our sample, divided by morphology, mass, and SFS. The first result that can be observed is that σ_{Scale} is generally higher than σ_{Shape}. This implies that within any classification scheme, the differences between ChEHs are primarily due to absolute differences in the value of the metallicity rather than to differences in enrichment rate.

Both σ_{Scale} and σ_{Shape} tend to increase from early morphological types toward late types, implying that earlier-type galaxies present a more similar evolution in general. For σ_{Shape} in particular, this is also true for more massive galaxies compared to less massive ones, an effect that is not as clear for σ_{Scale}. The Sd morphology bin exhibits a much larger σ_{Shape} and σ_{Scale} for the lowest-mass bin, which could be due to including Irr galaxies in the Sd bin.

When it comes to the SFS of the galaxies, the SFG tends to be more diverse than the RG. This is in line with the interdependence of SFS and morphology. A unique effect is observed for the dependence on mass: the correlation between σ_{Shape} and SFS disappears for the lowest-mass bin. This result can be interpreted from either the mass or from the SFS point of view. In the former, we conclude that low-mass galaxies have a wide distribution in terms of the shape of their ChEH, regardless of their SFS. In the latter, we conclude that the RG have a significant correlation between their mass and how diverse the shape of their ChEH is. The SFGs, on the other hand, have similar enrichment rates regardless of mass compared to the RG. Naturally, both interpretations are fully compatible, as they are simply different ways to view the same result.

5. Discussion

Three of the results presented in this article are especially relevant: How morphology shapes the MZR, the correlation between star formation and the flattening of the MZR, and the inversion of the metallicity gradient for low-mass galaxies.

It is well known that stellar mass is key in determining the shape of the MZR (e.g., Tremonti et al. 2004), but the role of morphology has not been studied consistently. Our results show that the global shape of the MZR is heavily influenced by morphology, with the low-mass range being similar to the MZR of Sd galaxies and the high-mass end being similar to E-Sa galaxies. This, of course, is not to deny the role of stellar mass: For all morphological types except perhaps Sd, stellar mass is still a strong regulator of how much and how quickly galaxies become enriched. The effects vary between morphological types, however. At the same stellar mass, an early-type galaxy will achieve a higher metallicity than a late-type galaxy, and it will do so more quickly. It appears, then, that both stellar mass and morphology are essential for understanding how galaxies become enriched.

The correlation we find between the SFS of galaxies and whether the MZR shows either a high- or low-mass flattening suggests that the processes that sustain or quench star formation
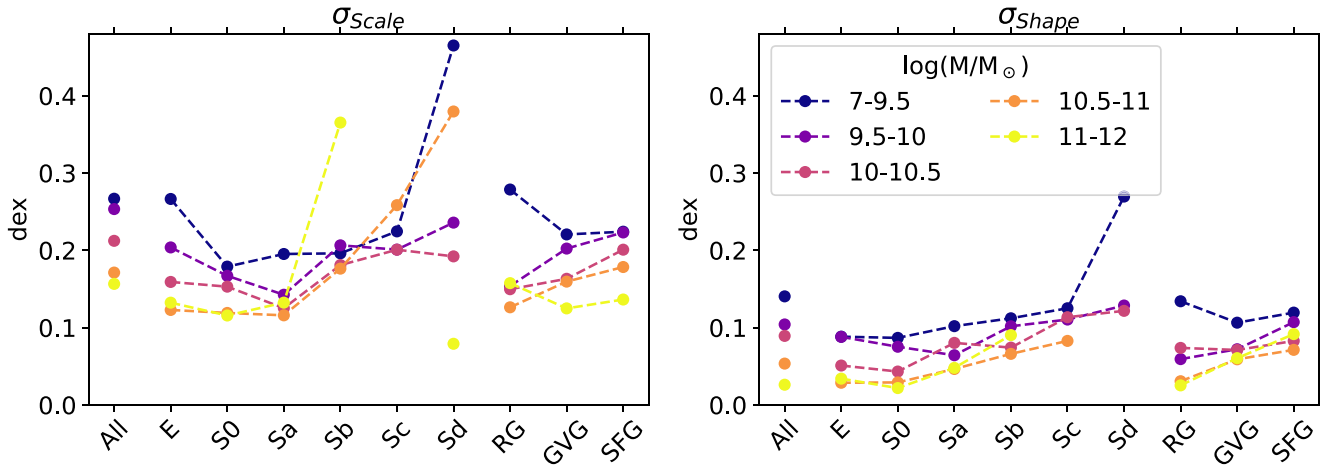
Figure 12. Comparison of the standard deviations of the ChEH for the different bins considered in this article, separated into the standard deviation due to the differences in the absolute value of the metallicity (σ_{Scale}) in the left panel and that due to a difference in the shape of the ChEH (σ_{Shape}) in the right panel.

are key in determining the chemical enrichment. The overall shape of the MZR has been generally linked to a correlation between the capacity for a galaxy to expel metals through outflows and the stellar mass as a proxy of the halo mass (e.g., Tremonti et al. 2004). In this scenario, the high-mass flattening occurs because above a certain stellar mass, outflows can no longer efficiently remove gas from the galaxy. Our results suggest that as long as a high SFR is sustained the outflows can still efficiently remove metals and it is only after the galaxy starts to become quenched that the higher potential curbs metal loss. The alternative scenario by Zahid et al. (2014) is also supported by our results. It describes the high-mass flattening as being the consequence of an equilibrium being reached between the production of metals by massive stars and the locking up of metals by low-mass stars. In this scenario, the RG and GVG would have reached this point earlier as a result of an earlier growth and lack of other mechanisms diluting the ISM.

Alternatively, hierarchical galaxy formation models can reproduce the MZR without requiring that metal loss determines its shape, but as a result of the star formation efficiency varying with mass (e.g., de Rossi et al. 2007; Finlator & Davé 2008). In these scenarios, our results would imply that as galaxies become quenched, the relation between mass and star formation efficiency changes. This would explain both the high- and low-mass flattening, but this change is difficult to determine using observational data.

Regarding the inversion of the metallicity gradient for lower-mass galaxies, there are high-redshift observational studies that find a substantial population of galaxies with a positive gradient (Cresci et al. 2010; Troncoso et al. 2014; Carton et al. 2018; Wang et al. 2019, 2020; Simons et al. 2021; Sharda et al. 2021), which does not appear in the local universe. One explanation for this is that the lower metallicity at the center is the result of merger-driven inflows of gas that enhance star formation at the center and simultaneously dilute the enriched gas there (see review by Maiolino & Mannucci 2019).

Our results are compatible with the observations as well as the interpretation, although a more detailed analysis of the stellar populations is needed to confirm the latter. The SFR at the center should be significantly enhanced for the LBT at which the gradient is inverted compared to the rest of the galaxy. This is necessary in order for merger-driven inflows to produce the apparent inversion in gradient rather than it being the result of secular evolution.

The values of the metallicity that the ChEHs (Figure 3) and MZR (Figure 4) reaches at its maximum are apparently low, as they do not reach solar metallicity even for very massive galaxies. There is a method-related issue that contributes to this, but the values are actually compatible with the literature. Previous works on the stellar MZR have generally used SDSS spectra, which are taken at the center of galaxies. Gallazzi et al. (2005; Figure 8), Panter et al. (2008; Figure 6), and Zahid et al. (2014; Figure 6) show a stellar MZR with a maximum around $[Z/H] \sim 0.1$–0.15. The MZR at the center in this article (Figure 10) has a maximum value of $[Z/H] = 0.12$, which is much better compatible than the value at Re. The aforementioned effect from the method is that the two-step averaging technique can lower the current metallicity values in order to preserve the shape of the average ChEH. This occurs when the galaxies at higher redshift have lower current metallicities on average, which is expected.

One of the ways that the results are model dependent lies in the choice of IMF. The results presented in this work use the Salpeter IMF (1955), but other IMFs are commonly used, such as those of Kroupa (2001), Miller & Scalo (1979), and Chabrier (2003.) The main difference between these and the Salpeter IMF is that the latter predicts a higher number of stars below $1\,M_\odot$ in a burst of star formation.

This can produce differences in our results at two stages of the analysis: (i) producing the templates used to fit the spectra and (ii) calculating the mass to light ratio. For (i) using an IMF other than Salpeter, and therefore having a lower fraction of low-mass stars, will make the template spectrum of a particular age and metallicity slightly less red, which when fitting them to observed spectra should induce the code to give a larger weight to templates labeled with higher metallicity and/or age values compared to templates computed using the Salpeter IMF. The resulting ChEHs would have a faster enrichment and higher values of the metallicity in general. However, while low-mass stars account for a large percentage of the total stellar mass, they contribute a much lower percentage of the luminosity of the stellar population, so the effects should not be too drastic in the computed templates. This would of course depend on the cutoff mass employed for the Salpeter IMF.

The other (ii) way that the IMF is used in the analysis procedure is to obtain the stellar mass by calculating the mass-to-light ratio, which is used to convert the observed luminosity

into stellar mass. Since low-mass stars make up the largest fraction of stellar mass, this has a significant effect on the values of the total stellar mass. For the properties shown in this article, the SFR would be affected in terms of its absolute value, but not in terms of its shape. The reason for this is that the IMFs differ only below 1 $M_\odot$, and none of the stars at this mass range are expected to have died since their birth. As such, a change in the relative amount of low-mass stars would change the SFR proportionally at all LBTs. The average metallicities should not be affected by the IMF choice at this step for the same reason.

It is important to note, however, that the universality of the IMF is not assured, with a growing body of evidence for its variation and even the concept of a scale-invariant universal IMF being questioned (see review by Hopkins 2018). This is of particular importance for the chemical content of galaxies, with abundance ratios between different elements not being consistent with a single, unchanging IMF (e.g., Arrigoni et al. 2010; Martín-Navarro et al. 2018; Fernández-Alvar et al. 2018; Horta et al. 2022).

The results presented in this article follow the general trend of the metallicity and as such are not as sensitive to a varying IMF as the abundance ratios. However, a variable IMF would still affect the results, with the same two mechanisms described above depending on the balance of low- and high-mass stars. The IMF is speculated to change over cosmic time and depending on physical properties such as stellar mass, gas pressure, morpholgical type, and SFR (e.g., Kroupa 2001; Fardal et al. 2007; Wilkins et al. 2008; Conroy & van Dokkum 2012; Ferreras et al. 2015; Yan 2021). This variation could affect the comparisons between the various bins considered in this article, although most behaviors reported here would require very specific IMF variations that correlate with both cosmic time and physical properties.

Martín-Navarro et al. (2015) used data and techniques similar to those used in this work on early-type galaxies to find a correlation between the high-mass slope of the IMF and the metallicity, such that the slope steepens for higher metallicities. This would make the templates redder, as described above (i), which would induce the code to select younger and less metallic templates in the fitting process. The net effect on our results should be a narrowing of the differences in metallicity between bins and ChEHs, with shallower enrichments in general.

The abundance ratios between elements have been observed to change within the Milky Way, suggesting that the IMF changes depending on the location (e.g., Yan et al. 2019; Yan 2021). Not taking this into account would mainly affect the metallicity gradients by changing their overall slope, but not necessarily their qualitative evolution in time.

This article constitutes an expansion of the work performed in the recent article CF21 for the CALIFA sample, but this time, using the larger MaNGA sample and a different set of stellar templates for the fit. It is important to compare the results of these studies, as the differences in sample, instrument, and method might be introducing artifacts into the results. To facilitate comparison between samples, we provide in Appendix C the same figures shown in this work, but using the GSD stellar library. Note that the range in metallicity values shown in these figures is not the same as that of the figures for the main results. The GSD library covers a narrower range of metallicity values (see Figure 15). The

analysis for the MaNGA sample with GSD is mostly equivalent to that of CF21, with some differences as described in Section 3.2.

The results with GSD are similar to those of CF21 both in terms of the absolute values of the metallicity and in terms of the shapes of the ChEH and MZR, with some notable exceptions. In CF21, Sa and S0 galaxies do not show a delay in enrichment in the MZR, unlike in this work. A careful comparison of the figures shows the reason for this: the change in slope only appears if we include the mass range below $10^{9.5}$ $M_\odot$, which is not represented in the CF21 version of this figure. The reason for this is that the selection criteria of CALIFA prefers objects with a higher inclination for low-mass disk galaxies, as they show a higher surface brightness. Our inclination criteria then remove most of these galaxies. E galaxies, which are populated in both samples, do show this effect. Another difference is the slope of the MZR for Sd galaxies, which appears flat in the CALIFA sample, but becomes negative for MaNGA galaxies. The progressive flattening of the MZR for later morphological types is similar between the two, but appears to be more dramatic in MaNGA.

One of the standout results in CF21 was that the SFG showed a clear convergence in the ChEHs. For the MaNGA sample, this effect is not as clear or distinct from the RG and GVG. It can still be observed to a degree for the three most massive bins (the two lowest bins have a steep growth for all SFS, which naturally produces a convergence toward the more massive bins) in that the gap between them is narrower at more recent cosmological times than in the past, whereas for RG and GVG, the gap between mass bins is constant.

The similarities of the results when using the same method implies that the differences between the CALIFA and MaNGA surveys (spatial and spectral sampling, sample selection, wavelength range, etc.) are not critical for the determination of the composition of the underlying stellar populations using the spectral synthesis technique. The method, on the other hand, plays a key role in determining the age and metallicity of the populations, with the choice of stellar library being paramount (Cid Fernandes et al. 2014). This does not mean that using different libraries will drastically affect the general behaviors, at least qualitatively. Independently of whether we use GSD or MaStar, we observe that the more massive galaxies are both more metallic and become enriched faster than lower-mass galaxies. The same general conclusions are reached regarding early-type versus late-type galaxies.

The greatest differences between GSD and the MaStar libraries appear when we separate the galaxies into SFS bins (see above) and when we adopt the gradient slope to measure the metallicity at different radial distances.

In CF21, the separation between ChEHs narrowed from the center to the outskirts, such that (i) the different galaxy mass bins present a smaller difference in metallicity, and (ii) it shows that low-mass galaxies always had a positive metallicity gradient as opposed to high-mass galaxies. Figures 22 and 9 show the same result, the former for the GSD library, and the latter for the MaStar library. The ChEHs measured at the outskirts are practically identical in the outskirts for GSD, while for MaStar, there is still some segregation with mass. The ChEHs for the CALIFA sample at the outskirts show a segregation as well, so this is not only an effect of the stellar library. Indeed, the CALIFA sample covers a larger average galactocentric radius than MaNGA (as a result of the field of

view of the instrument and the sample selection), which combined with the narrower range in metallicity values of the GSD library can explain why the ChEHs measured in the outskirts of the MaNGA sample with GSD are less reliable.

A key difference arises between the results for GSD and MaStar for the metallicity gradient. For the GSD library, high stellar mass galaxies have negative (in-out) values of the metallicity gradient and low-mass galaxies have positive (out-in) values instead, for all cosmic times. For the MaStar library, however, all galaxies currently have a negative metallicity gradient (shallower for low-mass galaxies), but low-mass galaxies used to have a positive gradient, signaling a transition.

6. Conclusions

In this work, we present the chemical evolution history of galaxies in the MaNGA sample measured using the spectral synthesis technique. The method we employed allows us to analyze the same set of galaxies throughout cosmic time, which yields a more consistent evolution. We find that stellar mass segregates the ChEH of galaxies both in terms of the value of their metallicity and of how quickly they become enriched, with the more massive galaxies having higher metallicities and a quicker evolution.

This is in line with previous works, but the dependence on stellar mass becomes less important after we separate the sample into morphology bins. Whereas the earlier-type galaxies show a similar dependence on stellar mass, the later morphological types become progressively less dependent on mass. The signature for this effect is the global flattening of the MZR, which inverts for Sd galaxies. The delay in enrichment experienced by low-mass galaxies compared to the high-mass galaxies is also affected in a similar way.

We also compare the chemical evolution of galaxies depending on their SFS. For the ChEH, we find results consistent with the correlation between morphology and SFS, but the MZR shows a unique feature that only appears to depend on SFS: The high- and low-mass flattenings of the MZR (both of which appear for the full sample) are associated with either RG or SFG. The high-mass flattening appears in RG, but not in SFG, and vice versa for the low-mass flattening.

Another key result is found when comparing the ChEHs at the center and in the outskirts of the galaxies: We detect an inversion of the metallicity gradient such that galaxies below $10^{10}\,M_\odot$ switch from an outside-in growth to an inside-out one. Higher-mass galaxies either maintained inside-out growth throughout their lifetimes, or we are unable to observe the switch with our method, due to the lesser reliability of older populations in the spectral synthesis technique.

As a result of the averaging technique we employed, we can separate the variance in the ChEHs of the galaxy bins we employ into scale and shape. The first is the variance related to the difference in the current value of the metallicity, while the second is the variance related to how different the shapes of the ChEHs are. We find that in general, galaxies are more diverse in terms of the value of their metallicity rather than the rate of enrichment, and the variance grows for lower masses and later morphological types.

Appendix A
Using the Redshift Range to Obtain the Evolution of the MZR

Given the relatively wide MaNGA redshift range for a local survey ($z \sim 0.01$–0.15), we should be able to use the currently observed metallicities to measure at least some evolution in the MZR over recent cosmic times by dividing the sample into redshift bins. In Figure 13 we show the resulting evolution of the MZR using three redshift bins. We only use three bins as the vast majority of the galaxies are relatively nearby and the higher redshift range has a much lower number of galaxies. From lowest to highest redshift, the number of galaxies for each bin is 3072, 5374, and 625.

The narrow range in redshift removes much of the evolution seen in Figure 4, with the highest-redshift bin showing a very narrow range in stellar mass. This is the consequence of an implicit bias that is introduced by the redshift bins. MaNGA is a size-selected survey, meaning that galaxies are chosen so that they fit properly within the field of view of the instrument, and, as such, there is a correlation between the redshift and the physical size of the galaxies, which in turn produces a correlation between mass and redshift. This greatly shortens
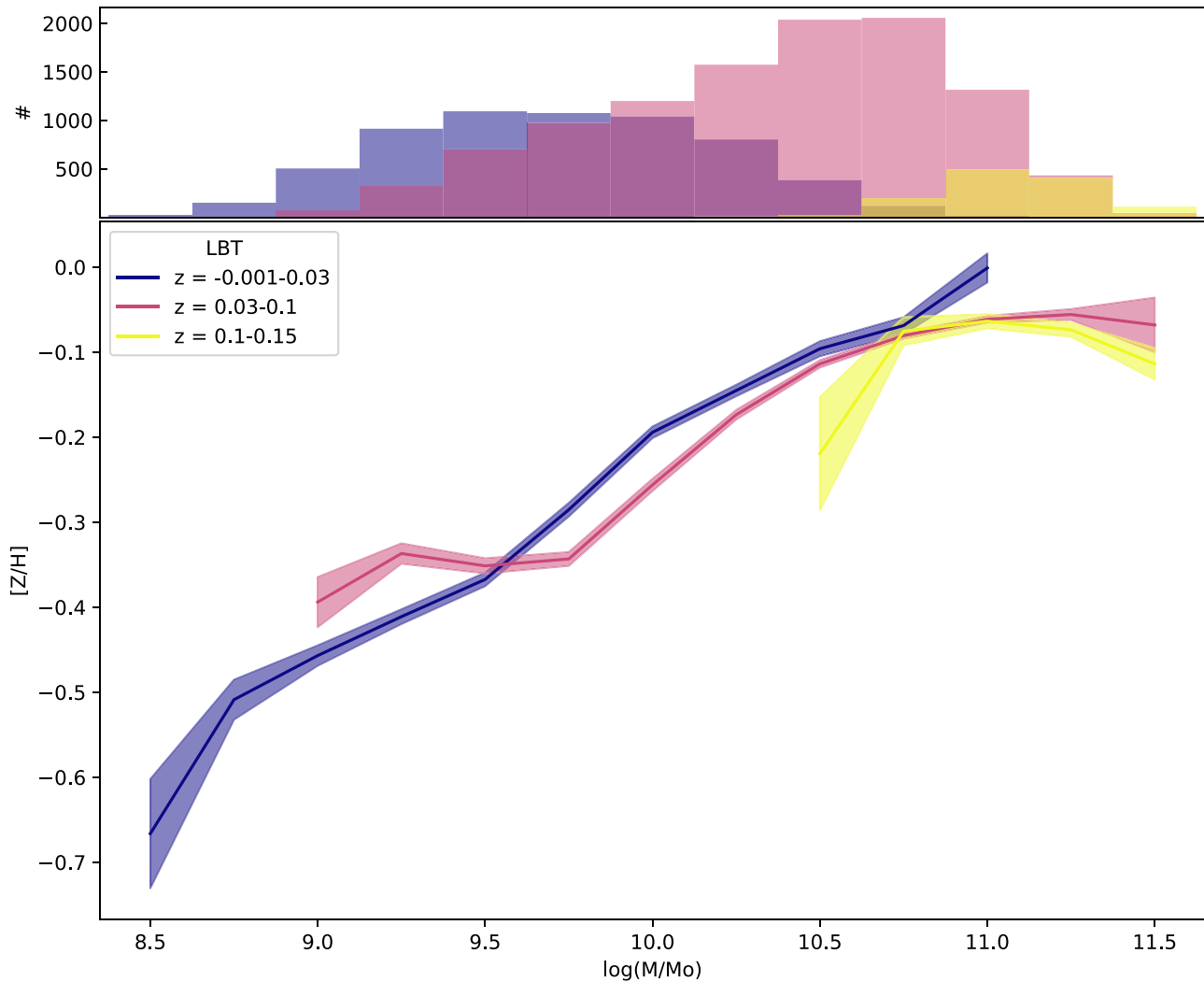
Figure 13. Evolution of the MZR (bottom panel) obtained by dividing the sample into redshift bins and averaging their currenly observed metallicity. The top panel shows the mass distribution of the galaxies for each redshift bin in the same colors.

the mass range that is sampled in the MZR for the highest-redshift bin.

At the low-mass end, there is also an apparent discrepancy with Figure 4, in which the galaxies below $\sim 10^{9.8}\ M_\odot$ appear to have experienced some sort of overall metal loss between the two most recent LBT (redshift) values. This is very likely to be another effect of an introduced bias. In addition to being size-selected, the MaNGA sample is also limited by surface brightness to ensure a good signal-to-noise ratio in the data. This has the effect of introducing a correlation between redshift and surface luminosity, which then also corresponds to a correlation between redshift and SFR, as the bright emission lines and young populations raise the overall surface luminosity of star-forming galaxies. Indeed, comparing the median SFR of the galaxies between 10^9 and $10^{9.8}\ M_\odot$ of the two lowest redshift bins shows that for the intermediate redshift, the galaxies have an SFR 2.4 times higher than the lowest redshift galaxies. As a result of this, the apparent metal loss is instead the consequence of the intermediate redshift showing the low-mass flattening of the MZR for SFG shown in Figure 8 and the lowest redshift following the general trend from Figure 4.

All of this should not give the impression that MaNGA is a biased sample, which it is not. The sample is carefully controlled

to be representative of the population of galaxies in the Local Universe, but this consistency can be broken if the sample is subdivided without accounting for possible biases that correlate internally with the property used to divide it. These results also illustrate the importance of controlling for the intrinsic selection effects that occur when observing galaxies at a high redshift in cosmological surveys. Spectral synthesis analysis such as the one presented in this article trades being free from these effects with the degeneracies intrinsic to the method, and as such, the two types of studies are highly complementary.

Appendix B
Stellar Library Sampling and Its Impact on the Results

There are four stellar libraries based on MaStar spectra that we considered for use in this study (LOG, LIN, MIX, and sLOG), as well as the GSD (GSD156; Cid Fernandes et al. 2013) stellar library. We use the latter in order to have a direct comparison between the results for the CALIFA sample presented in CF21 and those of this study (see Appendix B).

The results presented here are the first that use these stellar templates derived using the MaStar stellar library, and thus we performed tests regarding the suitable sampling of the parameter space, mainly that of the age of the populations.
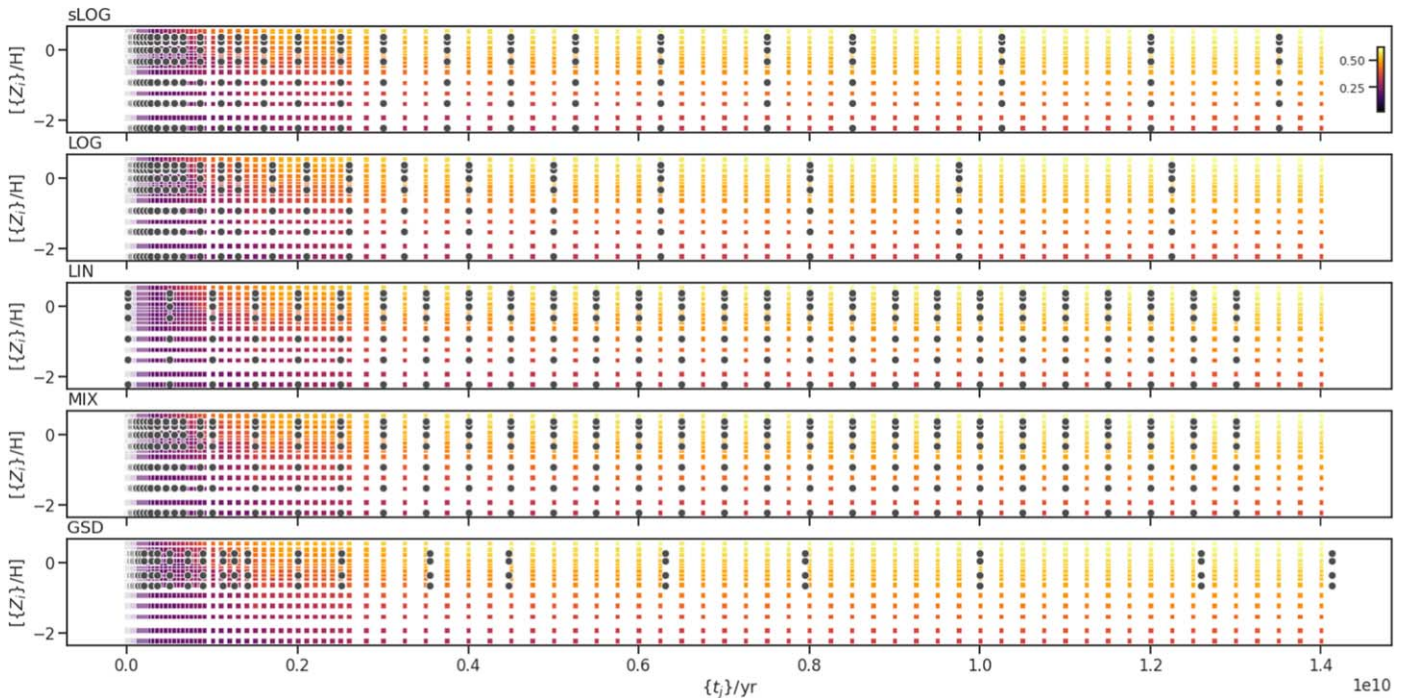
Figure 14. Representation of the sampling of the five stellar population templates considered in this paper, from top to bottom: sLOG, LOG, LIN, MIX, and GSD (black dots), in the metallicity vs age plane. The full templates for the MaStar stellar library without age and metallicity selection are also shown as colored squares. The color represents a function of the typical distance between them in terms of similarity of their spectra. We use this distance as a proxy for the degeneracy between these templates.

We present here a comparison and discussion of how the sampling in age affects the results.

The stellar template library we determined to be optimal is sLOG, and thus all results presented in the main body of the article were produced using this library. All four MaStar libraries comprise seven metallicities, ranging from $Z = 0.0001$ to $Z = 0.04$, which differ only in the age sampling. The LOG and LIN libraries sample the ages in a logarithmic and linear way, respectively. By construction, the first library samples the recent ages in a more refined way, while the second library samples the time in a homogeneous way. The MIX library samples the ages below 1 Gyr using the LOG distribution, and above this age, it uses the LIN distribution. Finally, the sLOG library adopts an intermediate procedure, sampling the age in multiplicative steps, in which the step is longer at older ages.

The GSD stellar template library comprises four metallicities, ranging from $Z = 0.004$ to $Z = 0.03$. Its age sampling is most similar to that of LOG and sLOG of the MaStar SSP libraries.

In Figure 14 we show a comparison between the five different libraries considered in this article and how their sampling differs. The age–metallicity values of the templates selected are represented as black dots over the full templates, which are represented as colored squares. The color represents a sort of distance between the templates in terms of how similar their spectra are, calculated using the chi-square between a template spectrum and those of its closest neighbors. The GSD templates are the only ones where the black dots representing the selection do not match the positions of the full templates, which is natural since it is the only SSP library that was not selected from the models of the MaStar stellar library.

We have measured the ChEH and MZR in the same manner as in the main body of the article using these different stellar libraries for the sake of completeness and as an exercise to assess the impact that the sampling has on our data.

In Figures 15 and 16 we compare the ChEHs and MZR that result from using different stellar template libraries.

The results are generally compatible between the libraries that are based on the same stellar spectra and that cover the same metallicity range (sLOG, LOG, LIN, and MIX), although there are some differences in the absolute values of the metallicity, with LOG showing the highest values and LIN the lowest. The GSD library has very different values for the metallicity for lower-mass bins, but this is a result of the narrower range in metallicity values that the library has compared to the others. However, the same general results regarding the shape of the ChEH can be seen, there is no saturation in terms of the metallicity, as one might expect. For example, the three lowest-mass bin metallicities in the MaStar libraries results are below the minimum values of the metallicity measured for the GSD library, but their ChEhs in the GSD library do not collapse to the same metallicity.

The LIN and MIX libraries show an odd feature in the ChEHs for the earliest LBT, an upturn of the metallicity toward earlier LBT, which sharply rises. The degree to which the metallicity would then have dropped from the earliest times, when galaxies were still in their growth phase, suggests that this is a spurious result. This is further reinforced by the fact that this feature disappears completely if the age sampling is changed. Both MIX and LIN have similar age samplings for the oldest populations. It is very likely that this spike in metallicity is the result of the degeneracies intrinsic to the method. Older populations need to have a wider sampling because their spectra change less over time. We recall that both libraries sample ages older than 1 Gyr in a linear way. This is strongly not recommended, since the differences between the spectra of
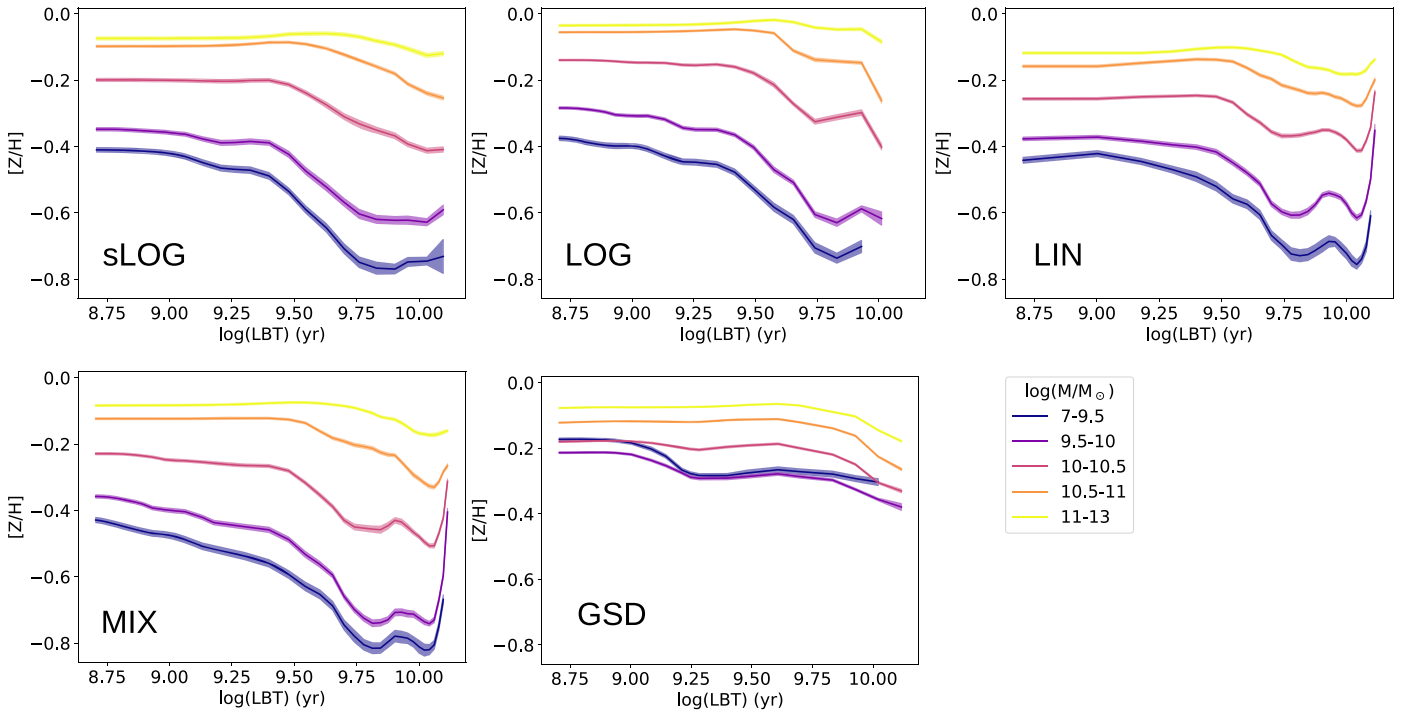
Figure 15. Comparison of the ChEH that results from using different stellar libraries. sLOG is the main library used in this work, while LOG, LIN, and MIX are libraries produced with the same spectra, but different samplings in age. Note that the GSD templates were not produced using the MaStar stellar library.
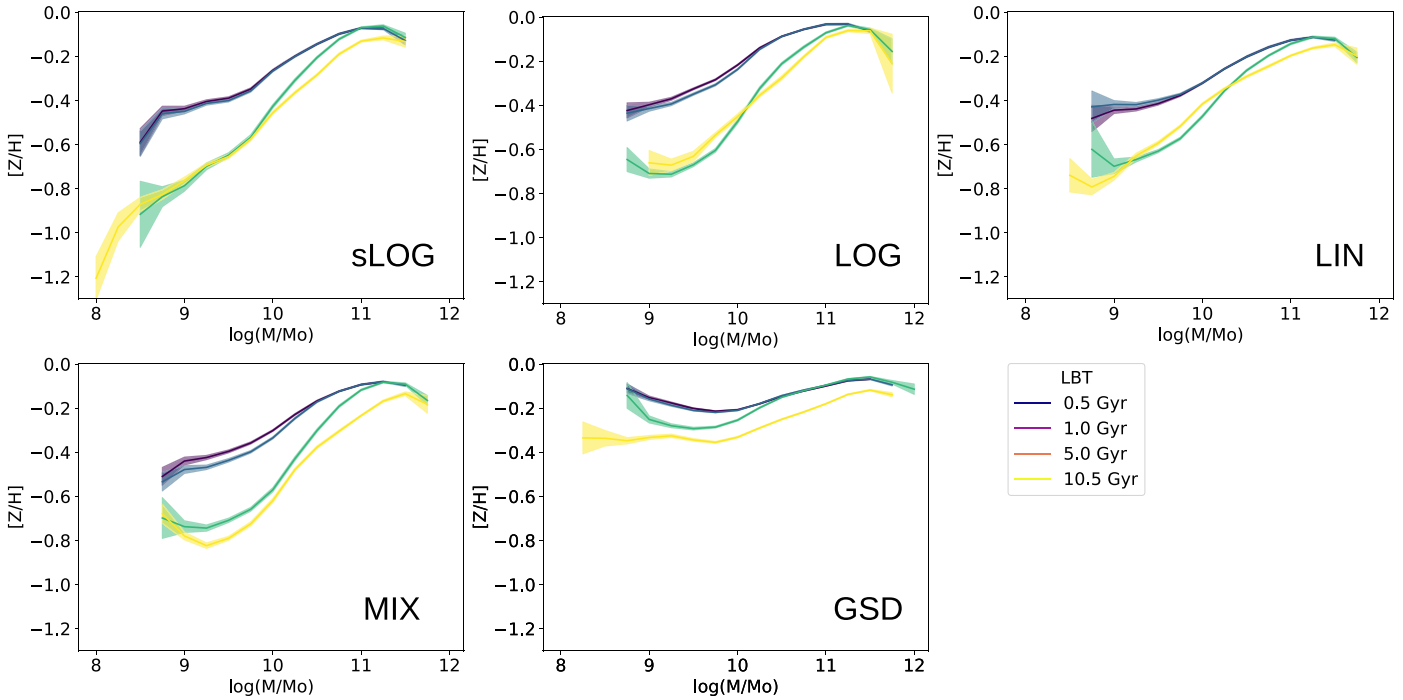

Figure 16. Comparison of the MZR evolution that results from using different stellar libraries. sLOG is the main library used in this work, while LOG, LIN, and MIX are libraries produced with the same spectra, but different samplings in age. Note that the GSD templates were not produced using the MaStar stellar library.

old stellar populations do not allow us to make a clean distinction between them (see Bruzual & Charlot 2003; Conroy 2013; Cid Fernandes et al. 2014).

The sLOG library was created to avoid this issue while adding some more data points for the older populations compared to LOG. We consider it to represent the best balance, showing consistent results with LOG, but it is better characterized for the further values of the LBT, as can be observed in Figure 15.

For the MZR, the results are mostly similar, except for those regarding the low-mass end of the MZR. All libraries except for sLOG have an inversion of the MZR at the very lowest

masses for LBT older than 1 Gyr. We have no explanation for this, but it should be noted that this happens for mass values that have a significantly lower number of galaxies and therefore a higher error in the determination of the MZR.

Appendix C
Using the GSD Library for a Direct Comparison between CALIFA (CF21) and MaNGA Results

As an aide in comparing the results shown in this work to those obtained using the CALIFA sample in CF21 we have reproduced all the figures in the main text of the article but using the GSD library in the spectral fitting process. This library is the one used for the analysis of the CALIFA sample

and by using it any differences between the CF21 figures and the ones in the main text should be attributed only to differences in the sample and instrument as well as any uncertainties intrinsic to the analysis method.

In Figure 17 we show the ChEHs and evolution of the MZR obtained from the full sample, while the following figures reproduce the comparison between the two types of bins considered in this article: morphology (Figures 18 and 19) and SFS (Figures 20 and 21).

Figures 22 and 23 show the difference of the ChEHs and MZR evolution resulting from measuring at different galacto-centric radii and Figure 24 compares the variance in the ChEHs for all the different bins (mass, morphology and SFS).
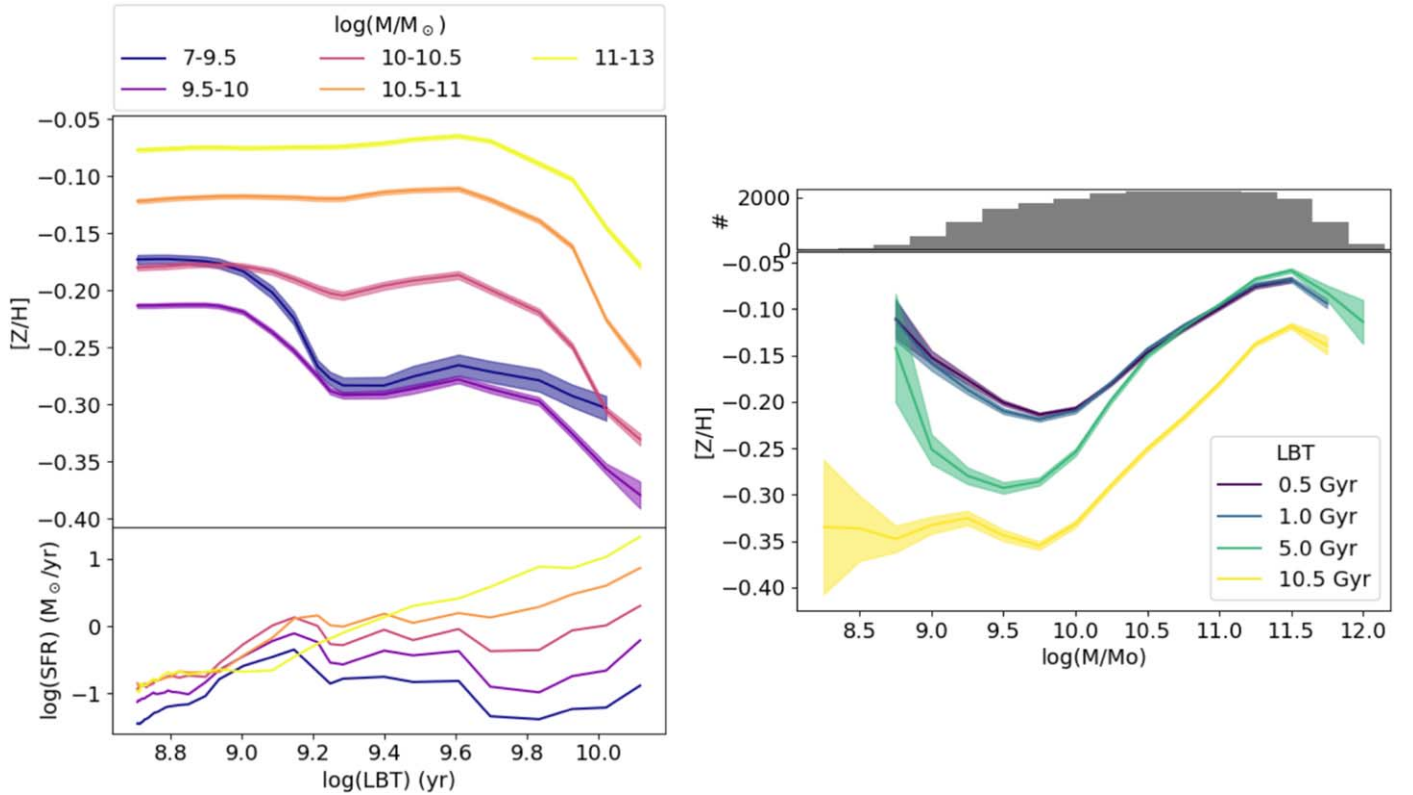

Figure 17. In the left panel, we show the evolution of the chemical enrichment along cosmic time for all galaxies in our sample for the GSD stellar library (bottom panel shows the SFH). In the right panel, we show the evolution of the MZR along cosmic times for the GSD stellar library (the top panel shows the distribution of the sample in currently observed stellar mass).
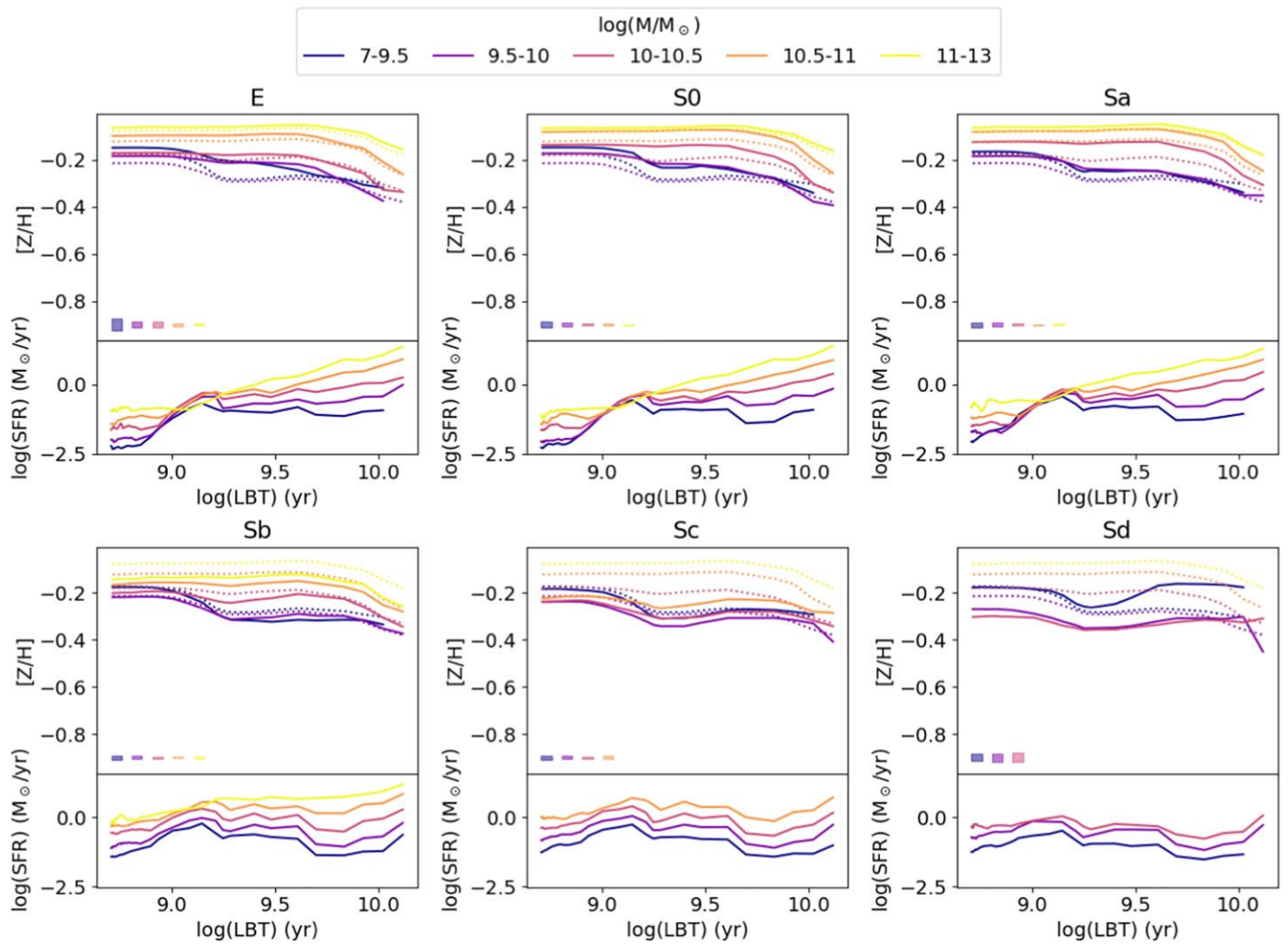
Figure 18. Evolution of the chemical enrichment for all galaxies in our sample for the GSD stellar library separated into morphology bins. In the bottom of each panel panel, we show the SFH.
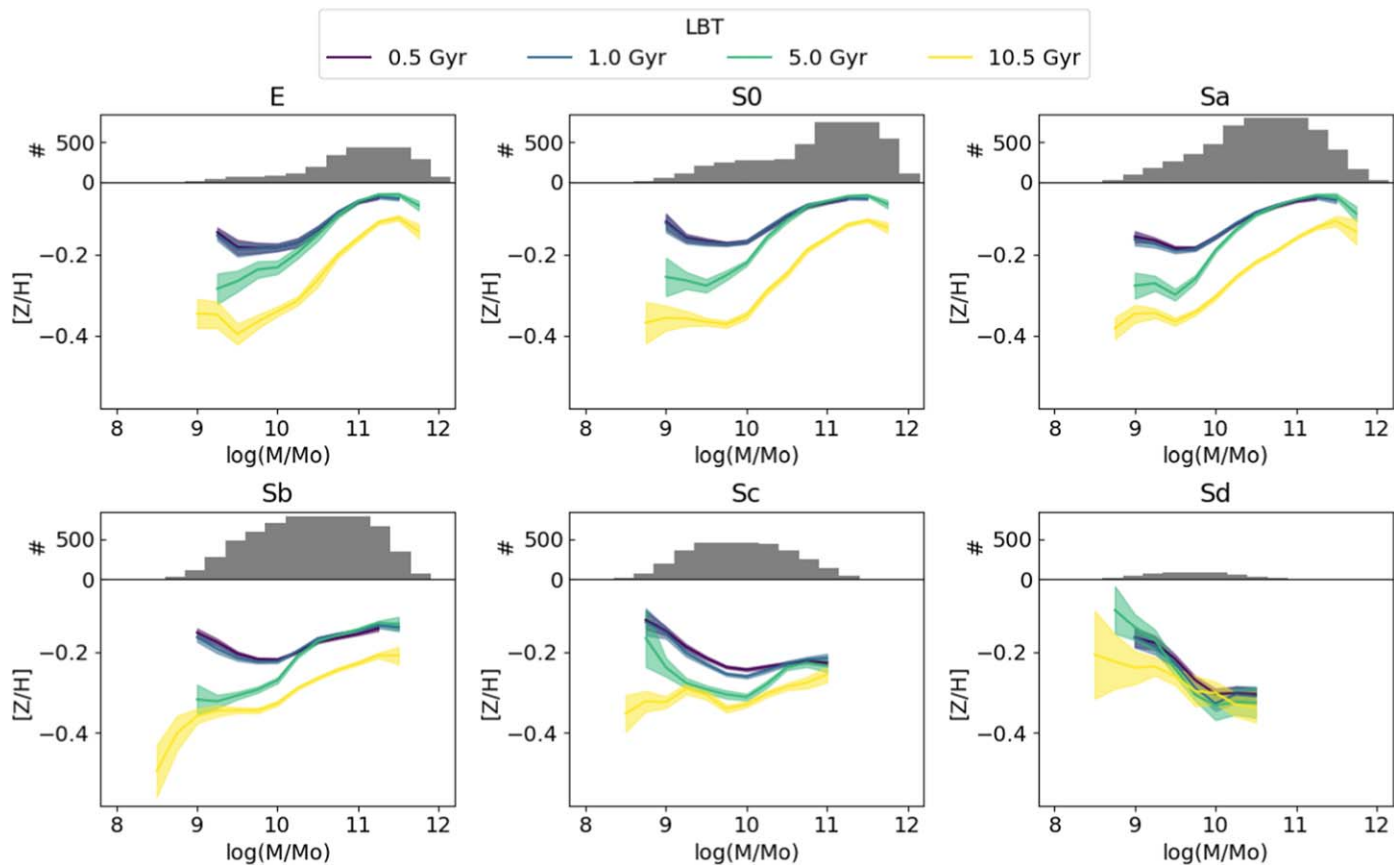
Figure 19. Evolution of the MZR for all galaxies in our sample for the GSD stellar library separated into morphology bins. In the top of each panel, we show the distribution of the sample in currently observed mass.
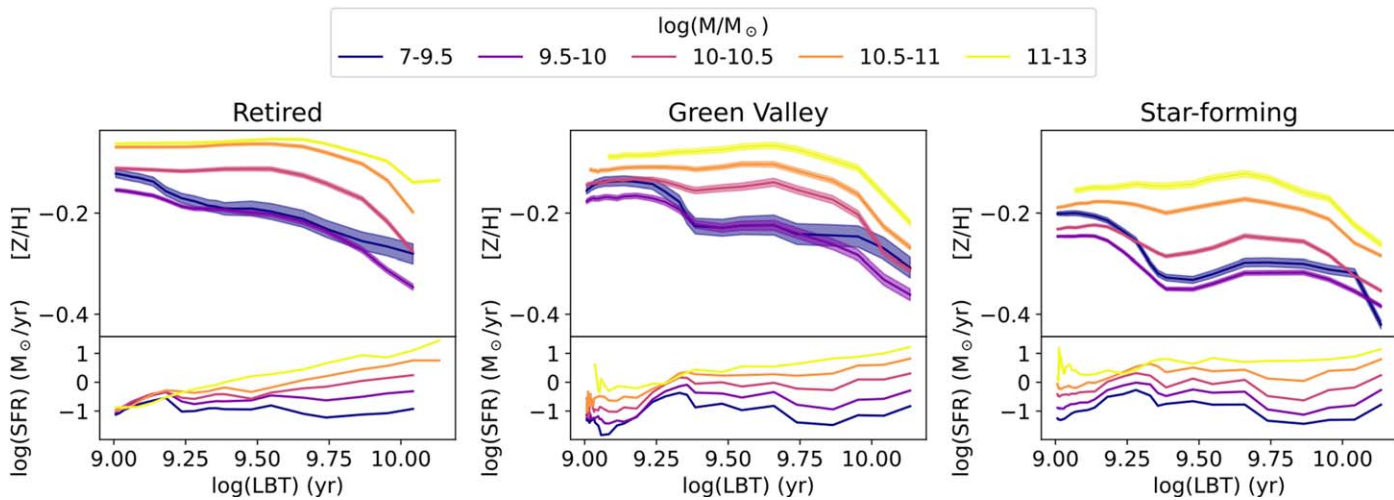

Figure 20. Evolution of the chemical enrichment for all galaxies in our sample for the GSD stellar library separated into SFS bins. In the bottom of each panel, we show the SFH.
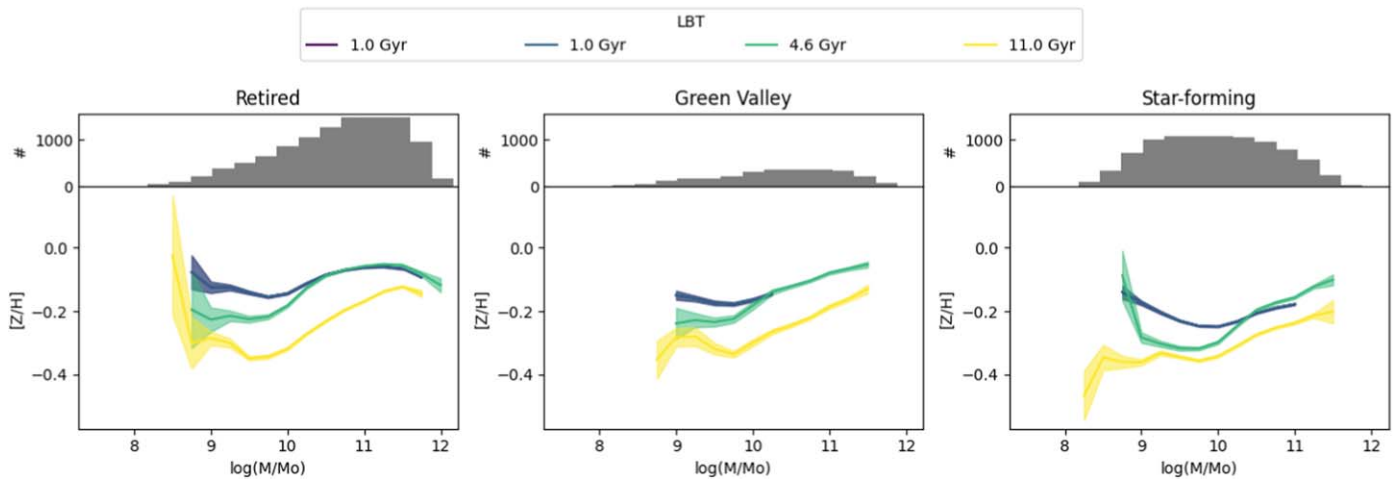
Figure 21. Evolution of the MZR for all galaxies in our sample for the GSD stellar library. In the top panel, we show the distribution of the sample in currently observed mass.
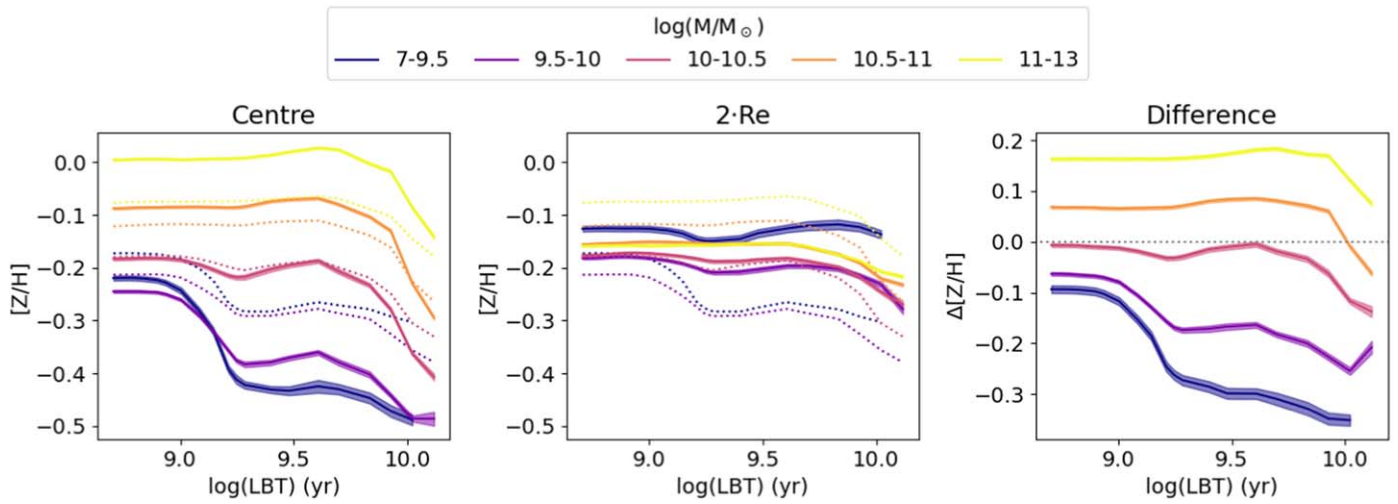

Figure 22. Evolution of the chemical enrichment for all galaxies in our sample for the GSD stellar library. In the bottom panel, we show the SFH.
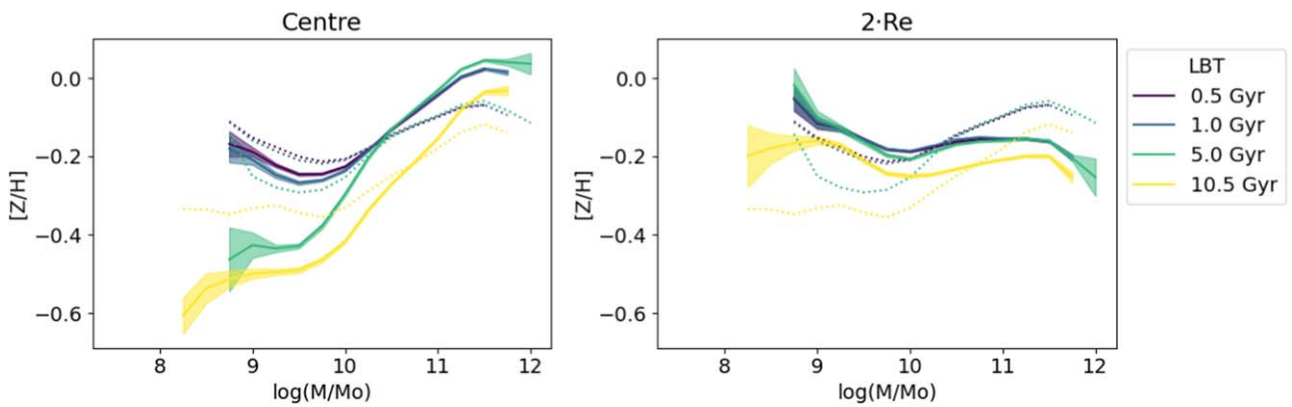

Figure 23. Evolution of the MZR for all galaxies in our sample for the GSD stellar library. In the top panel, we show the distribution of the sample in currently observed mass.
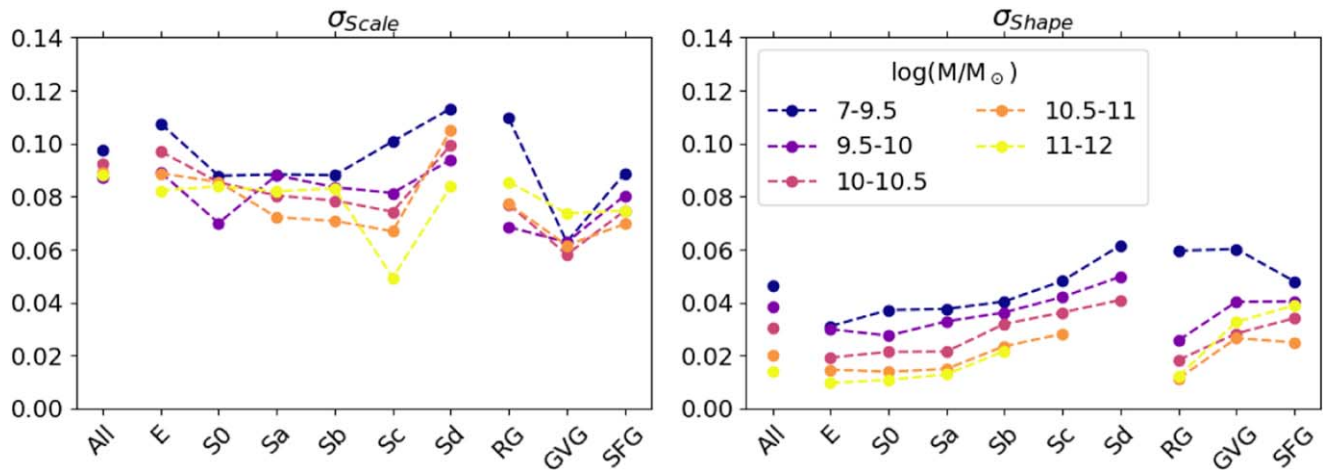
Figure 24. Comparison of the standard deviations of the ChEH for the different groups considered in this article using the GSD stellar library, separated into the standard deviation due to the absolute value differences in metallicity (scale) and that due to a difference in the shape of the ChEH (shape).

ORCID iDs

Artemi Camps-Fariña ● https://orcid.org/0000-0002-2555-1074

Sebastián F. Sánchez ● https://orcid.org/0000-0001-6444-9307

Alfredo Mejía-Narváez ● https://orcid.org/0000-0002-8931-2398

Eduardo Lacerda ● https://orcid.org/0000-0001-7231-7953

Leticia Carigi ● https://orcid.org/0000-0002-2023-466X

Gustavo Bruzual ● https://orcid.org/0000-0002-6971-5755

Paola Alvarez-Hurtado ● https://orcid.org/0000-0001-5514-7315

Niv Drory ● https://orcid.org/0000-0002-7339-3170

Richard R. Lane ● https://orcid.org/0000-0003-1805-0316

Guillermo A. Blanc ● https://orcid.org/0000-0003-4218-3944

References

Arrigoni, M., Trager, S. C., Somerville, R. S., & Gibson, B. K. 2010, MNRAS, 402, 173

Astropy Collaboration, Robitaille, T. P., Tollerud, E. J., et al. 2013, A&A, 558, A33

Barrera-Ballesteros, J. K., Sánchez, S. F., Heckman, T., Blanc, G. A. & MaNGA Team 2017, ApJ, 844, 80

Berg, D. A., Skillman, E. D., Marble, A. R., et al. 2012, ApJ, 754, 98

Blanc, G. A., Kewley, L., Vogt, F. P. A., & Dopita, M. A. 2015, ApJ, 798, 99

Blanc, G. A., Lu, Y., Benson, A., Katsianis, A., & Barraza, M. 2019, ApJ, 877, 6

Bresolin, F., Gieren, W., Kudritzki, R.-P., et al. 2009, ApJ, 700, 309

Bressan, A., Marigo, P., Girardi, L., et al. 2012, MNRAS, 427, 127

Bruzual, G., & Charlot, S. 2003, MNRAS, 344, 1000

Bundy, K., Bershady, M. A., Law, D. R., et al. 2015, ApJ, 798, 7

Camps-Fariña, A., Sanchez, S. F., Lacerda, E. A. D., et al. 2021, MNRAS, 504, 3478

Cano-Díaz, M., Ávila-Reese, V., Sánchez, S. F., et al. 2019, MNRAS, 488, 3929

Cano-Díaz, M., Sánchez, S. F., Zibetti, S., et al. 2016, ApJL, 821, L26

Carton, D., Brinchmann, J., Contini, T., et al. 2018, MNRAS, 478, 4293

Chabrier, G. 2003, PASP, 115, 763

Christensen, C. R., Davé, R., Brooks, A., Quinn, T., & Shen, S. 2018, ApJ, 867, 142

Christensen, C. R., Davé, R., Governato, F., et al. 2016, ApJ, 824, 57

Cid Fernandes, R., González Delgado, R. M., García Benito, R., et al. 2014, A&A, 561, A130

Cid Fernandes, R., Pérez, E., García Benito, R., et al. 2013, A&A, 557, A86

Conroy, C. 2013, ARA&A, 51, 393

Conroy, C., & van Dokkum, P. G. 2012, ApJ, 760, 71

Cresci, G., Mannucci, F., Maiolino, R., et al. 2010, Natur, 467, 811

Cullen, F., McLure, R. J., Dunlop, J. S., et al. 2019, MNRAS, 487, 2038

Dayal, P., Ferrara, A., & Dunlop, J. S. 2013, MNRAS, 430, 2891

de Rossi, M. E., Tissera, P. B., & Scannapieco, C. 2007, MNRAS, 374, 323

Drory, N., MacDonald, N., Bershady, M. A., et al. 2015, AJ, 149, 77

Espinosa-Ponce, C., Sánchez, S. F., Morisset, C., et al. 2020, MNRAS, 494, 1622

Fardal, M. A., Katz, N., Weinberg, D. H., & Davé, R. 2007, MNRAS, 379, 985

Fernández-Alvar, E., Carigi, L., Schuster, W. J., et al. 2018, ApJ, 852, 50

Ferreras, I., Weidner, C., Vazdekis, A., & La Barbera, F. 2015, MNRAS, 448, L82

Finlator, K., & Davé, R. 2008, MNRAS, 385, 2181

Gallazzi, A., Charlot, S., Brinchmann, J., White, S. D. M., & Tremonti, C. A. 2005, MNRAS, 362, 41

García-Benito, R., González Delgado, R. M., Pérez, E., et al. 2017, A&A, 608, A27

González Delgado, R. M., Cid Fernandes, R., García-Benito, R., et al. 2014, ApJL, 791, L16

González Delgado, R. M., García-Benito, R., Pérez, E., et al. 2015, A&A, 581, A103

Gunn, J. E., Siegmund, W. A., Mannery, E. J., et al. 2006, AJ, 131, 2332

Hernández-Toledo, H. M., Vázquez-Mata, J. A., Martínez-Vázquez, L. A., Choi, Y.-Y., & Park, C. 2010, AJ, 139, 2525

Hidalgo, S. L., Monelli, M., Aparicio, A., et al. 2013, ApJ, 778, 103

Hopkins, A. M. 2018, PASA, 35, e039

Horta, D., Ness, M. K., Rybizki, J., Schiavon, R. P., & Buder, S. 2022, MNRAS, 513, 5477

Husemann, B., Sánchez, S. F., Wisotzki, L., et al. 2010, A&A, 519, A115

Ibarra-Medel, H. J., Avila-Reese, V., Sánchez, S. F., González-Samaniego, A., & Rodríguez-Puebla, A. 2019, MNRAS, 483, 4525

Ibarra-Medel, H. J., Sánchez, S. F., Avila-Reese, V., et al. 2016, MNRAS, 463, 2799

Kashino, D., Renzini, A., Silverman, J. D., & Daddi, E. 2016, ApJL, 823, L24

Kennicutt, R. C. J., Bresolin, F., & Garnett, D. R. 2003, ApJ, 591, 801

Kewley, L. J., & Ellison, S. L. 2008, ApJ, 681, 1183

Kirby, E. N., Cohen, J. G., Guhathakurta, P., et al. 2013, ApJ, 779, 102

Kobayashi, C., Karakas, A. I., & Lugaro, M. 2020, ApJ, 900, 179

Kroupa, P. 2001, MNRAS, 322, 231

Lacerda, E. A. D., Sánchez, S. F., Cid Fernandes, R., et al. 2020, MNRAS, 492, 3073

Lacerda, E. A. D., Sánchez, S. F., Mejía-Narváez, A., et al. 2022, arXiv:2202.08027

Law, D. R., Cherinka, B., Yan, R., et al. 2016, AJ, 152, 83

Lee, H., Skillman, E. D., Cannon, J. M., et al. 2006, ApJ, 647, 970

Leethochawalit, N., Kirby, E. N., Ellis, R. S., Moran, S. M., & Treu, T. 2019, ApJ, 885, 100

Lilly, S. J., Carollo, C. M., Pipino, A., Renzini, A., & Peng, Y. 2013, ApJ, 772, 119

López-Sánchez, Á. R., Dopita, M. A., Kewley, L. J., et al. 2012, MNRAS, 426, 2630

Lu, Y., Blanc, G. A., & Benson, A. 2015, ApJ, 808, 129

Ma, X., Hopkins, P. F., Faucher-Giguère, C.-A., et al. 2016, MNRAS, 456, 2140

Maiolino, R., & Mannucci, F. 2019, A&ARv, 27, 3

Mannucci, F., Cresci, G., Maiolino, R., Marconi, A., & Gnerucci, A. 2010, MNRAS, 408, 2115

Martín-Navarro, I., Vazdekis, A., Falcón-Barroso, J., et al. 2018, MNRAS, 475, 3700

Martín-Navarro, I., Vazdekis, A., La Barbera, F., et al. 2015, ApJL, 806, L31

Matteucci, F. 2012, Chemical Evolution of Galaxies (Berlin: Springer)

Miller, G. E., & Scalo, J. M. 1979, ApJS, 41, 513

Minchev, I., Chiappini, C., & Martig, M. 2013, A&A, 558, A9

Minchev, I., Chiappini, C., & Martig, M. 2014, A&A, 572, A92

Panter, B., Heavens, A. F., & Jimenez, R. 2003, MNRAS, 343, 1145

Panter, B., Jimenez, R., Heavens, A. F., & Charlot, S. 2007, MNRAS, 378, 1550

Panter, B., Jimenez, R., Heavens, A. F., & Charlot, S. 2008, MNRAS, 391, 1117

Pérez, E., Cid Fernandes, R., González Delgado, R. M., et al. 2013, ApJL, 764, L1

Pérez-González, P. G., Rieke, G. H., Villar, V., et al. 2008, ApJ, 675, 234

Pérez-Montero, E., & Díaz, A. I. 2005, MNRAS, 361, 1063

Pharo, J., Malhotra, S., Rhoads, J., et al. 2019, ApJ, 874, 125

Rosales-Ortega, F. F., Sánchez, S. F., Iglesias-Páramo, J., et al. 2012, ApJL, 756, L31

Salpeter, E. E. 1955, ApJ, 121, 161

Sánchez Almeida, J., Elmegreen, B. G., Muñoz-Tuñón, C., & Elmegreen, D. M. 2014, A&ARv, 22, 71

Sánchez, S. F. 2006, AN, 327, 850

Sánchez, S. F. 2020, ARA&A, 58, 99

Sánchez, S. F., Avila-Reese, V., Hernandez-Toledo, H., et al. 2018, RMxAA, 54, 217

Sánchez, S. F., Barrera-Ballesteros, J. K., López-Cobá, C., et al. 2019, MNRAS, 484, 3042

Sánchez, S. F., Barrera-Ballesteros, J. K., Sánchez-Menguiano, L., et al. 2017, MNRAS, 469, 2121

Sánchez, S. F., Pérez, E., Sánchez-Blázquez, P., et al. 2016a, RMxAA, 52, 171

Sánchez, S. F., Pérez, E., Sánchez-Blázquez, P., et al. 2016b, RMxAA, 52, 21

Sánchez, S. F., Rosales-Ortega, F. F., Iglesias-Páramo, J., et al. 2014, A&A, 563, A49

Sánchez, S. F., Rosales-Ortega, F. F., Jungwiert, B., et al. 2013, A&A, 554, A58

Sánchez, S. F., Walcher, C. J., Lopez-Cobá, C., et al. 2021, RMxAA, 57, 3

Sánchez-Blázquez, P., Ocvirk, P., Gibson, B. K., Pérez, I., & Peletier, R. F. 2011, MNRAS, 415, 709

Sánchez-Blázquez, P., Rosales-Ortega, F. F., Méndez-Abreu, J., et al. 2014, A&A, 570, A6

Schaye, J., Crain, R. A., Bower, R. G., et al. 2015, MNRAS, 446, 521

Sharda, P., Krumholz, M. R., Wisnioski, E., et al. 2021, MNRAS, 502, 5935

Simons, R. C., Papovich, C., Momcheva, I., et al. 2021, ApJ, 923, 203

Smee, S. A., Gunn, J. E., Uomoto, A., et al. 2013, AJ, 146, 32

Stasińska, G., Vale Asari, N., Cid Fernandes, R., et al. 2008, MNRAS, 391, L29

Tremonti, C. A., Heckman, T. M., Kauffmann, G., et al. 2004, ApJ, 613, 898

Troncoso, P., Maiolino, R., Sommariva, V., et al. 2014, A&A, 563, A58

Urrutia, T., Wisotzki, L., Kerutt, J., et al. 2019, A&A, 624, A141

Walcher, J., Groves, B., Budavári, T., & Dale, D. 2011, Ap&SS, 331, 1

Wang, X., Jones, T. A., Treu, T., et al. 2019, ApJ, 882, 94

Wang, X., Jones, T. A., Treu, T., et al. 2020, ApJ, 900, 183

Wilkins, S. M., Hopkins, A. M., Trentham, N., & Tojeiro, R. 2008, MNRAS, 391, 363

Yan, C.-S., & Wang, J.-M. 2010, ApJ, 725, 2359

Yan, R., Tremonti, C., Bershady, M. A., et al. 2016, AJ, 151, 8

Yan, Z. 2021, arXiv:2112.08141

Yan, Z., Jerabkova, T., & Kroupa, P. 2019, A&A, 632, A110

Yates, R. M., Henriques, B., Thomas, P. A., et al. 2013, MNRAS, 435, 3500

York, D. G., Adelman, J., Anderson, J. E. J., et al. 2000, AJ, 120, 1579

Zahid, H. J., Bresolin, F., Kewley, L. J., Coil, A. L., & Davé, R. 2012, ApJ, 750, 120

Zahid, H. J., Dima, G. I., Kudritzki, R.-P., et al. 2014, ApJ, 791, 130

Zhuang, Z., Kirby, E. N., Leethochawalit, N., & de los Reyes, M. A. C. 2021, ApJ, 920, 63